Journal of Energy Storage 98 (2024) 112863

Contents lists available at ScienceDirect

Journal of Energy Storage

journal homepage: www.elsevier.com/locate/est

Research papers

Manufacturing of tabless cylindrical lithium-ion cells: Quantifying the influence of cell dimensions and housing material via process-based cost modeling

Hendrik Pegel [a,*], Adrian Grimm [b], Christian Frey [c], Volker Seefeldt [d], Sabri Baazouzi [e], Dirk Uwe Sauer [a]

[a] Chair for Electrochemical Energy Conversion and Storage Systems, Institute for Power Electronics and Electrical Drives (ISEA), RWTH Aachen University, Campus-Boulevard 89, 52074 Aachen, Germany
[b] Karlsruhe Institute of Technology KIT, Straße am Forum 8, 76131 Karlsruhe, Germany
[c] Welding and Joining Institute (ISF), RWTH Aachen University, Pontstr. 49, 52062 Aachen, Germany
[d] SFT – Consulting, Am Meisenberg 29, 34431 Marsberg, Germany
[e] Fraunhofer Institute for Manufacturing Engineering and Automation IPA, Nobelstr. 12, 70569 Stuttgart, Germany

ARTICLE INFO

Keywords:
Lithium-ion batteries
Large-format cylindrical cells
Tabless electrode
Housing manufacturing
Impact extrusion
Battery cost optimization

ABSTRACT

The cost saving potential of large-format tabless cylindrical lithium-ion cells has been widely recognized since Tesla announced their plans to produce and BMW has confirmed to adopt this type of cells due to economic benefits among other reasons. However, a quantification and deep analysis of the cost reduction emerging from enlarged dimensions and further innovations such as different housing materials has not been reported in scientific literature so far. In this study, the process steps of manufacturing a large-format tabless cylindrical cell are examined and published in detail for the first time. A model is established that incorporates all manufacturing steps as a function of cell dimensions and choice of housing material. It was found that enlarging the dimensions from the conventional 2170 to the 4680 format achieved a cost reduction of 10.9% for two main reasons. First, the manufacturing cost per kWh decreases due to certain manufacturing steps being directly dependent on the number of cells produced. Second, the cells volumetric energy density itself increases due to a better volume efficiency of the active material share which further decreases the number of cells required. Introducing aluminum housings offers additional cost saving potential of as much as 2.5% of the total cost of 4680 cells due to an efficient backwards impact extrusion manufacturing process and lower cost of the aluminum raw material compared to nickel-plated steel.

1. Introduction

Large-format cylindrical lithium-ion cells have been widely discussed in recent years since Tesla announced their 4680 cell with 46 mm diameter and 80 mm height [1]. Especially the tabless electrode design [2] enables cells with larger dimensions through enhanced current collecting and thermal pathways [3–6]. Recent works reported extreme fast-charging performance [7,8] and the influence of cell dimensions and housing material on the structural components and the thermo-electrical performance [9] of large-format cylindrical cells with innovative tab design. Enhanced energy density and performance are however only some of the reasons automotive manufacturers plan to utilize cylindrical cells with tabless electrodes and enlarged dimensions. According to Tesla they expect to achieve a double-digit percentage reduction in total cost by introducing 4680 cells [1]. BMW reported they aim to cut overall electric vehicle cost by 25% [10] and cut battery system cost by as much as 50% [11] with the introduction of their 'new-class' vehicles in 2025 that utilize 46xxx tabless cylindrical cells with 46 mm diameter and varying height [12]. A number of cell manufacturers such as Samsung [13], BAK Battery [14] and Rimac [15,16] further announced development of 46xxx cells with 46 mm diameter and custom height. Scientifically studying and understanding the cost saving potential of enlarged dimensions is thus necessary to enable development of tabless cylindrical cells with optimized trade-off between enhanced energy density, increased performance and reduced cost which will speed up the adoption of e-mobility and environmentally friendly means of transportation.

* Corresponding author.
E-mail address: hendrik.pegel@rwth-aachen.de (H. Pegel).

https://doi.org/10.1016/j.est.2024.112863
Received 15 March 2024; Received in revised form 19 May 2024; Accepted 7 July 2024
Available online 27 July 2024

There is plenty of literature available for manufacturing pouch cells and prismatic cells [17–21]. In contrast, studies that investigate manufacturing cost of cylindrical cells are sparse, based on conventional dimensions such as commercial 18650 and are outdated regarding recent innovations such as the tabless electrode design [22,23]. Quinn et al. [24] pointed to the cost saving potential of enlarging the cell dimension years prior to Teslas announcement of introducing the 4680. A cost reduction per kWh was also theorized by Waldmann et al. [25] recently. However, to the best of our knowledge, no scientific study was able to quantify these thoughts. This is not surprising as manufacturing cost models required to achieve this are already notoriously difficult to parameterize for a given cell format and design, let alone including variable dimensions. A first manufacturing cost model of this kind was recently introduced by Boerner et al. [26] who reported the impact of the tabless design on electrode manufacturing including a 'flag forming' step based on the 2170 format. They however did not investigate the complete manufacturing process including assembly and finishing and did not analyze the influence of varying diameters and heights.

Further, to the best of our knowledge there exists no single study that investigates the manufacturing process and cost of state-of-the-art cylindrical cell housings. This process is however a key piece for fully understanding the cost saving potential of larger dimensions as the number of housings required per kWh decreases [24]. Introducing aluminum housings rather than common steel housings further enhances the thermo-electrical performance through better electrical and thermal conductivity [7] and allows for tighter packing density [27]. Understanding the implications of aluminum housings on all aspects of battery systems including cost is therefore of great interest to make informed decisions about the choice of housing material.

In this paper, a scientific deep dive into state-of-the-art manufacturing technology of large-format cylindrical cells with innovative tab design is reported. Different manufacturing processes for tabless jelly rolls and innovative new housing designs are explained in detail. For the first time, a manufacturing cost model is developed for all existing and new manufacturing steps that were introduced in recent years as a function of cell dimensions and housing material. A sensitivity study quantifies the impact of the tabless electrode design, the cell dimensions and the housing material on the manufacturing cost of large-format tabless cylindrical cells. The results are suitable to serve as input for multi-objective battery system optimization.

2. Analysis of the manufacturing process of tabless cylindrical lithium-ion cells

2.1. Influence of large-format cylindrical cell technology on manufacturing

Cell designs of conventional 18650 and 2170 cells were mostly unchanged for more than a decade and little innovation has taken place in this field. Deep drawn cell housings were combined with crimped endcaps that contain safety devices such as a current-interrupt-device (CID), integrated burst discs and positive temperature coefficient (PTC) sealings [28]. The manufacturing processes for these type of cells are well known and optimized by the manufacturers. Meanwhile, large-format cylindrical cells have introduced a number of further innovations in addition to enlarged dimensions and introducing the tabless electrode design. Especially the design of the cell bottom and top endcaps is crucial for achieving the desired performance and safety behavior. However, apart from what has been reported in our previous studies [7,9,27,29] little information is documented about sophisticated mass-produced large-format tabless cylindrical cell designs other than what is known about the first generation of the Tesla 4680 [30,31]. This could lead to the fallacy of believing the Tesla cell design is the only design that will be present in all future 46xxx cells. In reality, a variety of different cell designs will emerge in the future that are heavily optimized towards delivering specifically targeted trade-off between multiple properties when integrated into different battery systems. Baazouzi et al. [31] recently introduced a categorization of different tabless cylindrical cell designs that provides a first overview about the many different viable approaches. Especially the type of cooling system and the cooled surface [9], possibly mechanical support to prevent side-wall breaches [29] during thermal runaway and the role of the cell housing of absorbing shear stress are key to consider before choosing a certain cell design. For example, the Tesla 4680 model 3 battery is combined with a surface cooling just like the previous generations of 18650 and 2170 batteries across all Tesla vehicles. The main advantage of this type of cooling compared to the highly effective bottom cooling [32] for tabless cylindrical cells with large diameters and regular height such as the 4680 almost certainly does not lie in enhanced thermo-electrical behavior [9,32], but rather in the opportunity of having complete freedom of designing the cell endcaps and tabless jelly roll to endcap connection [31]. Most importantly, the venting mechanism can be shifted to the side opposite to the terminal which is connected to the busbars. This allows for contacting negative and positive poles on one side of the cell and venting towards the other side. This enhances the reliability of the venting mechanism and drastically reduces the risk of voltage flashovers and electric arcs [29]. The safety of cylindrical cells has already been one of the major advantages compared to pouch and prismatic cells [27,29] due to the defined venting area and low energy content per cell. The above described cell design further improves this advantage. Especially combined with a strong mechanical support between the cells and low thermal conductivity of the interstitial material it is expected that cylindrical cells will achieve greater thermal propagation safety compared to other cell formats. However, implementing the venting mechanism into the cell bottom imposes restrictions on designing the electrical connection between the tabless jelly roll and the cell bottom around the vent area. On the other hand, by introducing the tabless electrode design a bottom cooling approach is now feasible [7,9,32] due to the overall drastically reduced electrical resistance and ohmic losses [3,5,28,33] as well as better thermal connection between the cell ends and the cell bottom [7]. Contrary to a surface serpentine cooling, for a bottom cooling setup the thermo-electrical performance is largely independent of the cell diameter as the ratio of cooled surface to cell volume and the effective cell length in the direction of the main heat flow remains constant [9]. When using a cooling plate however, the venting path at the bottom of the cell is blocked and the venting mechanism cannot be separated from the terminal. However, this allows for complete freedom of applying the best manufacturing technology for minimizing the thermal resistance between the jelly roll and the cell bottom, which is a key for maximum performance with bottom cooling [7]. As can be concluded from publicly available CT-Scans [31] the Tesla 4680 for example is not suited for a bottom cooling approach for many reasons. Especially the large air gap between the tabless jelly roll and the crimped cell bottom [30] poses a thermal insulation in axial direction which would cause dire performance [7].

To summarize, it is important to understand that not only the cell dimensions and tab designs but rather every single structural cell component must be considered and optimized for maximum performance and safety. OEMs and cell manufacturer must optimize the cell design towards their specific application and need. For the reasons outlined above completely different cell designs and therefore manufacturing technologies are required when combining large-format tabless cylindrical cells with different battery system designs. As can be concluded from this fact, manufacturing lines will vary across different manufacturers and flexibility is needed to satisfy future customer demands. In this paper, a manufacturing line for one specific novel large-format tabless cylindrical cell design that is optimized for a bottom cooling setup is assumed to analyze and understand the influence of cell dimensions and housing materials.

2.2. Reference cell for further analysis and model parameterization

A state-of-the-art tabless cylindrical cell with 10 Ah capacity and dimensions between common 2170 with about 5 Ah [34] and 4680 cells with about 22.5 Ah [30,31] is used as a reference baseline for model parameterization. The reference cell has a $LiNi_xMn_yCo_zO_2$ (NMC, x > 0.8) cathode, SiO_x-C anode with carbon nanotubes (CNT), DMC:EC:EMC electrolyte and an Al_2O_3 coated separator. The housing is made from an extruded Al-3003 aluminum-manganese tube with laser welded endcaps, the copper and aluminum current collector foils are wound with continuous overhangs and joined to a collector plate on both sides. The same cell has been subject to extensive research in a number of previous studies including thermo-electrical-electrochemical behavior [7–9], geometric aspects of the structural components [9], experimental thermal runaway and thermal propagation characterization with focus on the cylindrical aluminum housings [29] as well as analysis of measures to prevent thermal propagation [27]. Further detailed analysis and modeling of the manufacturing techniques, structural components and active material composition will be done in the following sections.

2.3. Manufacturing of large-format tabless cylindrical cells

This section analyses the steps of manufacturing large-format tabless cylindrical lithium-ion cells at the example of a cell design that is optimized towards a bottom cooling approach and derived from the cell design of the reference cell introduced above. A difference between the reference cell and the cell design assumed here is that the housing of the reference cell is made from an extruded aluminum tube with openings on both sides [7,9,27,29] while in this work the housing is assumed to be produced by deep drawing for steel or impact extrusion for aluminum to form a can with a single opening on one side. Fig. 1 visualizes the set of key steps involved in manufacturing such a state-of-the-art tabless cylindrical lithium-ion cells with deep drawn steel housing or impact extruded aluminum housing, laser welded endcaps and ultrasonic welded bottom collector plate. Note that the process may differ for different housing materials, tabless design approaches and the depicted steps are just one way to manufacture a tabless cylindrical cell. The manufacturing steps that are well documented and similar to those of former single tab cells are analyzed based on existing literature. Analysis of the newly introduced novel manufacturing steps that are not yet documented in scientific literature is based on the experience of the authors that include academia, research institutions and independent industry experts.

2.3.1. Categorizing the manufacturing steps

Literature usually categorizes manufacturing of lithium-ion cells including cylindrical formats as follows [35]:

- A) Electrode preparation
- B) Assembly
- C) Finishing

This categorization neglects manufacturing steps of cylindrical housings and treats those as given external input as is usually assumed in previous studies that analyzed manufacturing cost of cylindrical cells [22]. This makes it impossible to analyze the influence thereof as a function of dimensions, choice of material and manufacturing technology. Therefore, for this study we suggest an extended and slightly different categorization that is visualized in Fig. 1:

- A1) Tabless jelly roll manufacturing
- A2) Housing manufacturing
- B) Assembly
- C) Finishing

This categorization is based on the thought of which steps can be performed in parallel and simultaneously before components from different steps are required to continue manufacturing. Even though in reality those steps are likely not performed within the same facility, this categorization has proven to be intuitive and easy to understand. In this case, the tabless jelly roll including tabless winding and collector plate welding (A.1) may be produced simultaneously to the housing (A.2) which is manufactured depending on the material, cell and endcap design. The tabless jelly roll is then inserted into the housing to finalize the assembly (B). Subsequent cell finishing is classified identical to existing literature (C).

2.3.2. A1) Tabless jelly roll manufacturing

The impact of introducing new innovative tab designs and new housing manufacturing methods on the jelly roll manufacturing steps needs to be closely analyzed with respect to the actual kind of tabless design and manufacturing technique applied. First, the mixing process and preparation of the slurry is generally unaffected by the subsequent tab design. As for the influence on coating and drying, a distinction between two different common tab approaches is required. In the past, either an additional tab piece was welded to the metal foils or the foils were cut such that the created overhang itself acted as a tab. These two approaches are referred to as 'welded tabs' or 'foil tabs' in the literature, respectively [25]. For welded tabs it was necessary to position a tab within the middle of the electrode leaving a blank spot and posing a requirement for an intermittent coating process [26]. For a tabless jelly roll, this is no longer necessary and a continuous coating process without requirements for blank spots is applicable. For manufacturing foil tabs, precisely controlled cuts had to be performed before winding such that the overhangs appear at the desired positions within the subsequent spirally wound shape of the jelly roll [25]. A recent study by Boerner et al. [26] compared the manufacturing cost of single tab jelly rolls to tabless jelly rolls based on Teslas notching design [30,31]. This design requires equidistant 'flags' that have to be cut into the metal foils similar to the described former foil tab designs. The authors found that the additional step which they call 'flag forming' increases manufacturing cost [26]. The reference cell that acts as a baseline for this study utilizes an advanced manufacturing technique that does not require flag forming. The collector plates are laser welded directly onto the metal foil overhangs in a 90° angle. This erases the need for a flag forming step. In-detail explanation and modeling of this weld is supplied in the following sections of this study. For detailed analysis of the structural components of the reference cell the reader is referred to [9].

Assuming the 90° jelly roll to collector plate welding technique, apart from the now continuous coating process all steps of mixing, coating and drying, recovery of N-Methyl-2-pyrrolidone (NMP) for cathode only, calendering, cutting and vacuum drying are unaffected by the tab design. Changes arise after the vacuum drying process. Fig. 1 left depicts the following winding and welding process for manufacturing a tabless jelly roll. The winding process may now happen with continuous copper and aluminum foil overhangs on both sides. There is no more need to focus on the placement of the welded single tabs or the alignment of the multi foil tabs such that they can be collectively welded together after winding. After winding so called 'collector plates' are welded onto the foil overhangs in a 90° angle [7,9,27,29] as explained above. The collector plates usually have holes to allow for electrolyte insertion, degassing of gaseous byproducts from SEI formation or electrolyte degradation and most importantly to allow venting gas to built up pressure and blow up the venting mechanism before thermal runaway initiation. Also, for ultrasonic welding of the bottom collector plate the electrode needs to be inserted through the hollow core such that the top collector plate must have a central hole [9]. The collector plates for the 90° technique have grooves that are pressed into the ends of the jelly roll and laser spot welded to the foils. This ensures that the collector plates are well attached and in contact with the

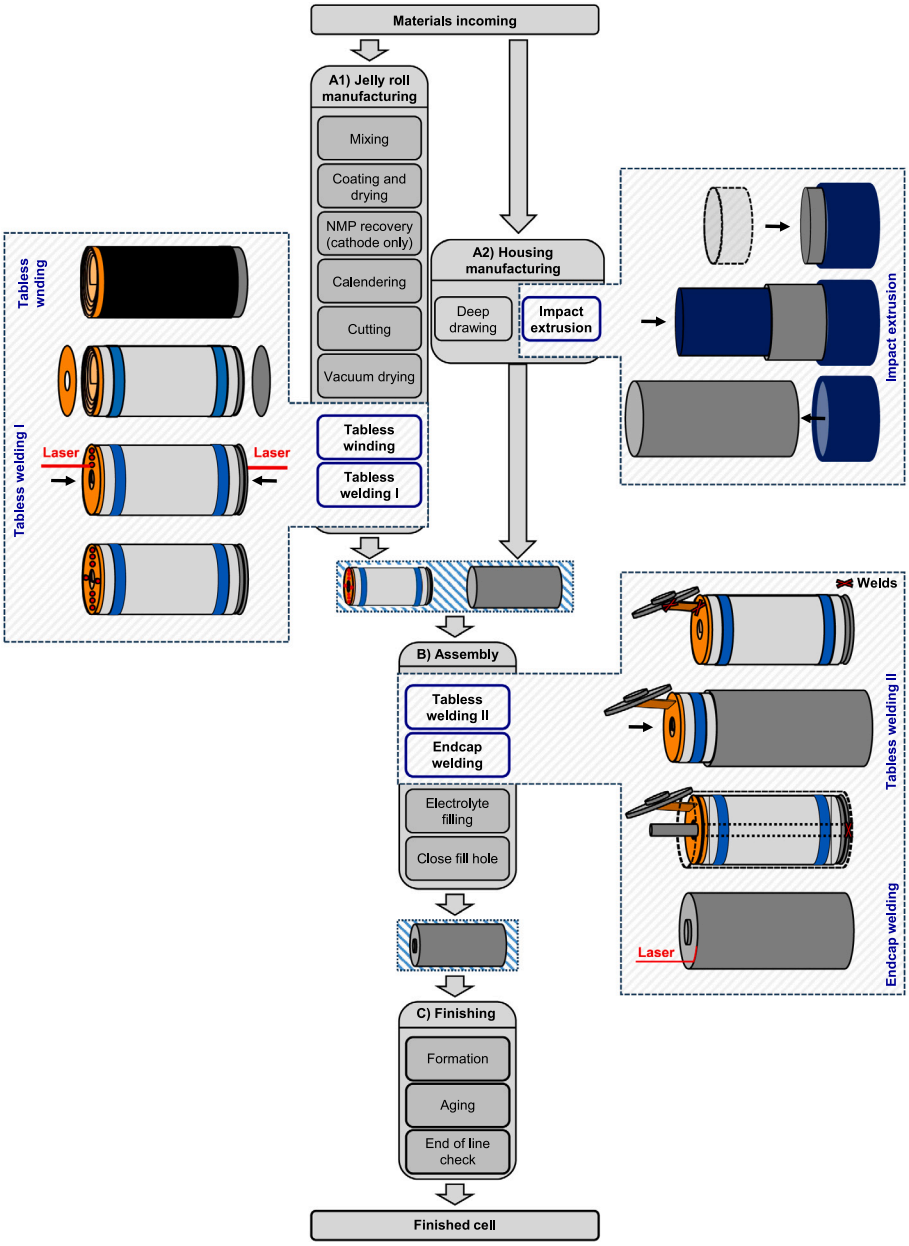

Fig. 1. Manufacturing process of large-format tabless cylindrical lithium-ion cells including can and endcap. Top left: manufacturing of tabless jelly roll with collector plates (A1), top right: deep drawing (steel) or impact extrusion (aluminum) of the can (A2), middle: cell assembly (B) and bottom: finishing (C). Note that this is just one of the many ways to manufacture a tabless cylindrical cell.

foils, ideally over a large cross section to minimize internal resistance. This type of weld erases the need for flag forming [26]. However, it is exceptionally difficult to perform and control with highest quality during mass production. Very thin metal foils with thickness less than 8 µm of copper and less than 15 µm of aluminum have to be carefully pressed against the collector plates with precisely controlled force.

The overall process of tabless winding and tabless current collector plate welding can be viewed in a video released by Tesla [36]. Note that their tabless jelly roll depicted in this video is however manufactured with the flag forming approach [26] rather than the 90° welding technique.

2.3.3. A2) Housing manufacturing

Housings of lithium-ion cells provide the first level of thermal and mechanical protection for the cell interior components [37]. An ideal housing would act as a barrier for oxygen and vapor, be mechanically stable, resistant to internal pressure, chemically resistant to the electrolyte, electrically and thermally conductive, suitable for welding and bonding and be light and easy to manufacture. For decades, cylindrical cell housings for 18650 and 2170 have mostly been made of deep drawn nickel-plated steel cans combined with crimped endcaps [37,38] to meet these demands. Greatly initiated by the Tesla battery day in 2020 [1] a lot of innovation is taking place in this area nowadays that has not yet been documented in scientific literature. One of these trends is the introduction of aluminum rather than steel housings. Especially for large-format tabless cylindrical cells such as 4680 or 46xxx cooling becomes more challenging compared to common 18650 and 2170 as the surface-to-volume ratio decreases [9]. Materials with higher electrical and thermal conductivity such as aluminum are thus desirable to reduce ohmic losses caused by the current flow within the can for one-sided contacting and to enhance heat dissipation. Especially the latter also contributes to increased thermal propagation resilience, possibility

of decreased cell-to-cell spacing and tighter packing density on battery system level [27]. Recent studies further reported extreme fast-charging performance of novel tabless cylindrical cells with housings made from extruded aluminum tubes [7,9]. However, manufacturers are still hesitant to introduce cylindrical aluminum housings even though they have been state-of the art for prismatic hardcase housings for a long time [38].

For cylindrical housings, usually aluminum of the essentially pure 1-series (1050, 1200) or aluminum-manganese alloy 3-series (3003, 3005) are used. Aluminum housings may theoretically be produced on regular deep drawing machines also used for steel cans. However, as aluminum has better flow behavior due to less mechanical strength new possibilities for manufacturing arise. Based on the experience of the authors, applying a backwards impact extrusion process has many advantage such as having less manufacturing steps involved, less tooling is needed, a faster manufacturing speed can be achieved and the process in general is highly flexible compared to conventional deep drawing of steel housings. Natori et al. [39] recently formulated similar thoughts with regard to the application of backwards impact extrusion for aluminum housings of cylindrical lithium-ion cells. Further, different housing heights may be produced with the same tool by inserting different thicknesses of raw work pieces. For multistep deep drawn steel housings, every single tool for each step has to be adjusted to manufacture housings with different heights even if the diameter remains constant. This is a huge disadvantage compared to backwards impact extrusion with regard to the supposed new standard cell format of 46xxx with constant 46 mm diameter and varying height [9].

The endcap of 18650 and 2170 steel cells is usually crimped onto the open end of the cell can [37] left after deep drawing. In this case the endcap usually contains safety devices such as burst discs PTC sealings [28]. This is an expensive design as the endcap is made of five different individual parts [22]. For regular deep drawn 18650 and 2170 cells, the endcap is responsible for roughly $2/3^{rd}$ of the housing cost based on the experience of the authors. Further, the crimped design is rather complex and does not use the available height of the cell efficiently which decreases the achievable coating height of the jelly roll and thus the cells energy density. Also, the venting mechanism is commonly located at the same side as the central terminal and electrical contacting, making it difficult to ensure the desired safety behavior due to the risk of voltage flashovers and electric arcs [29]. Instead, laser welding a flat endcap for both steel and aluminum is cheaper to produce and has better packing efficiency. In this case, safety features such as the venting mechanism may be directly integrated for example by engraving predetermined breaking lines [29]. This design also allows for easy one-sided contacting and to realize the venting mechanism on the opposite side of the terminal resulting in safer overall system design. The reference cell used for parameterization of the modeling frameworks in our previous studies [7,9,29] is such an example of a tabless cylindrical cell with novel aluminum tube housing, double sided laser welded endcaps and venting separated from the electrical contacting. The Tesla 4680 combines a deep drawn steel housing with one crimped endcap on the cell bottom and the addition of a central terminal on the top side of the cell [30,31].

To reveal the influence of different material choices and manufacturing techniques on the manufacturing cost, the housing in the modeling part of this study is assumed as either a common 5-stage deep drawn steel can or an impact extruded aluminum can with one laser welded endcap in both cases. Fig. 1 right depicts the basic impact extrusion process which includes placing a cylindrical raw work piece into a die and forming of the can by punching. For detailed explanation of this process the reader is referred to the study of Natori et al. [39].

2.3.4. B) Assembly

After the tabless jelly roll with welded collector plates is finished, one of the collector plates is joined to a central terminal. In case of a aluminum can, the copper collector plate, in case of a steel can, the aluminum collector plate. As depicted in Fig. 1 bottom right (tabless welding II) this may be realized by laser welding a metal connector to both components. Other approaches may realize this connection with a 'pin' as is done in the Tesla 4680 [30,31]. Afterwards, the jelly roll is inserted into the can and an ultrasonic welding process is applied via a welding electrode that is inserted through the hollow core. This step is similar to the manufacturing of single tab cells except not a single tab but the collector plate is spot welded to the bottom center of the can. Experiments have confirmed that it is indeed possible to create a successful laser weld from outside the cell can through the bottom without the need to insert an electrode through the cell core. This weld allows for larger coating heights and welding area which reduces the ohmic resistance and enhances the thermal pathway, but is however more challenging to control. In the future, it is likely that this kind of weld becomes more common as manufacturers learn to control and optimize this approach.

In a final step the endcap is laser welded to the can and the cell is ready for vacuum drying and electrolyte filling. If an aluminum tube with openings on both sides was used, both ends of the jelly roll can be joined with a metal connector before laser welding the endcaps to the open ends. The manufacturing steps following endcap welding remain unchanged, electrolyte filling and closing of the fill hole.

2.3.5. C) Finishing

The finishing steps of formation, aging and end of line (EOL) check are generally unaffected by the new cell designs and remain unchanged to how they were performed in the past.

3. Modeling

In this section, all existing and newly introduced manufacturing steps are mathematically modeled using a process-based cost model (PBCM). In the following sections, the term total cost refers to the sum of the manufacturing cost and material cost. The model is implemented in MATLAB.

3.1. Approach: process-based cost model

The PBCM is a bottom-up approach that calculates material cost and manufacturing cost analytically on the basis of technical and operational parameters [17,40,41]. A product is first broken down into its individual components. These components are divided into the resources and processes required [17]. A number of different cost types such as material, equipment, building, maintenance, labor, energy and fixed overhead cost are then allocated to those resources and processes in order to produce the desired amount of products [22]. Previous studies have used this approach to investigate manufacturing of prismatic [21] and cylindrical cells [22] due to its ability to reveal which parameters contribute most to the total cost among other advantages [17].

Parameterizing a detailed PBCM for manufacturing of lithium-ion cells however is notoriously difficult as the values needed are usually hard to come by and often kept secret by manufacturers. Especially for novel large-format tabless cylindrical cells a race between manufacturers to produce the best cell for the least cost is underway [13,14,16,42,43] and little information is publicly shared. In this study, parameterization was made possible by a close collaboration of academia, research institutions, leading independent industry experts and the support of cell manufacturers.

The PBCM established in this study includes a geometrical model, a process model, an operations model and a financial model. This study focuses on exploring the influence of the tabless electrode design, enlarged dimensions and new housing materials and manufacturing techniques. This is mainly considered in the geometrical model that describes the structural components and energetic properties as well as the process model which adjusts the individual manufacturing steps

to produce exactly the cell described by the geometrical model. The operations and financial model have more generic character and are not directly affected by the primary variables investigated. This study however aims to provide full parameterization of each submodel in order to enable other researchers to expand on this basis in the future. Therefore, in the following sections of the main text the geometrical model and the process model with strong focus on parameterization subject to the novel tabless electrode design as well as the dependency on cell diameter, cell height and housing material is explained in-detail. This includes the highlighted steps of tabless winding, tabless welding I, tabless welding II, endcap welding and the housing manufacturing in Fig. 1. Further parameterization can be found in the Appendix. With the information from the main text and the Appendix combined, the complete parameterization of the PBCM is disclosed with exception of the reference cells active material geometrical properties as those are subject to confidentiality. This provides other researchers the opportunity to qualitatively reproduce the results, adjust the parameterization and extend the model to solve the many additional future research questions that must be answered and which go beyond the scope of this work.

3.2. Geometrical model

The geometrical model provides a description of the cell under consideration such that the material masses can be determined and the manufacturing processes can be adjusted in order to produce cells with a certain specific geometrical description. At this point this description must be developed as a continuous function of the variables investigated in this study, namely the cell diameter, the cell height and the housing material.

In our previous study such a model was developed that describes the geometry of the cells structural components including wall thickness, core diameter, inactive height and jelly roll trajectory as a function of cell dimensions and housing material subject to certain defining load-cases [9] based on the tabless reference cell. For this study, the manufacturing line is modeled with regard to exactly this variable cell geometry. Therefore, the geometrical model from [9] is first adopted as is. This assures that all results are obtained on a consistent basis and can be used to generate understanding of all aspects of large-format cylindrical cell technology at the example of a common reference cell.

Table 1 summarizes the equations adopted from [9]. The trajectory of the layers $r(\varphi)$ and the total length of the jelly roll ΔS is calculated as a function of the layer thickness t_{layer}, core diameter d_{core} and housing wall thickness t_{wall} according to Eqs. (1)–(9). The core diameter d_{core} is primarily determined based on the risk of core collapse (Eq. (7)). The wall thickness t_{wall} is derived from the raw material yield strength and experimental data of the cells venting behavior in order to provide the required burst pressure during thermal runaway (Eqs. (8)–(9)). Thicknesses of anode coating t_{ano}, copper foils t_{cu}, cathode coating t_{ca}, aluminum foils t_{al} and separator t_{sep} are parameterized based on the active material present in the tabless reference cell. The coated height of the jelly roll h_{coat} is determined by a constant inactive offset on anode side $h_{inact,ano}$ and cathode side $h_{inact,ca}$ that is required for integrating the tabless electrode design and to prevent the heat generated by the laser from damaging the active material during welding of the collector plates (Eqs. (10)–(12)). The cell energy E_{cell} is calculated from the length of the jelly roll ΔS, layer thickness t_{layer}, coating height h_{coat} and specific volumetric energy density $e_{vol,act}$ of the active material (Eq. (13)). The specific volumetric energy density $e_{vol,act}$ of the active material present in the reference cell was identified as 852 Wh l^{-1}. For deeper explanations of the formulas the reader is referred to the original source [9].

For the PBCM some additions to the geometrical model in Table 1 are required. First, the volumes V_j of anode coating, cathode coating, copper foils, aluminum foils and separator are calculated with the length of the layer trajectory ΔS, the thicknesses t_j and heights h_j of each of the listed components according to Eq. (14).

$$V_j = \Delta S(\varphi_{start}, \varphi_{end}) t_j h_j \tag{14}$$

The true solid coated material volume $V_{solid,j}$ within each electrode j is calculated with the porosity $\phi_{electrode,j}$ of anode and cathode according to Eq. (15). The absolute pore volume therefore calculates according to Eq. (16). The porosity was determined by experimental analysis of the active material present in the reference cell.

$$V_{solid,j} = V_j(1 - \phi_{electrode,j}) \tag{15}$$

$$V_{pores,j} = V_j \phi_{electrode,j} \tag{16}$$

The solid coated material volume is further divided into the volumes V_i of material i by multiplying with the gravimetric share constant ψ_i according to Eq. (17). This includes SiO_x, graphite, nickel, manganese, cobalt, binder, carbon black, CNT, carboxymethyl cellulose (CMC), styrene-butadiene rubber (SBR) and polyvinylidene fluoride (PVDF). The gravimetric share constant ψ_i of each of the above listed materials was determined by extensive chemical analysis of the active material present in the reference cell.

$$V_i = V_{solid,j} \psi_i \tag{17}$$

The required electrolyte volume is calculated according to Eq. (18). Here, $V_{pores,tot}$ is the total pore volume of anode coating, cathode coating and separator that requires being completely filled with electrolyte according to Eq. (19). An additional overfill factor $\kappa_{electrolyte}$ that considers free electrolyte volume outside of the pores is considered, $\kappa_{electrolyte} > 1$. The overfill factor $\kappa_{electrolyte}$ was determined from gravimetric analysis of the reference cell.

$$V_{electrolyte} = V_{pores,tot} \kappa_{electrolyte} \tag{18}$$

$$V_{pores,tot} = V_{pores,ano} + V_{pores,ca} + V_{pores,sep} \tag{19}$$

The volumes of the housing components divided into deep drawn or impact extruded can volume V_{can}, endcap volume V_{endcap} and terminal volume V_{term} are calculated according Eq. (20), Eq. (21) and Eq. (22), respectively. Note that the wall thickness and therefore housing component volume is a function of the choice of housing material according to the formulas in Table 1 [9].

$$V_{can} = \pi(r_{cell}^2 - (r_{cell} - t_{wall})^2)(h_{cell} - t_{endcap}) + \pi(r_{cell} - t_{wall})^2 t_{bot} \tag{20}$$

$$V_{endcap} = \pi(r_{cell}^2 - r_{term}^2) t_{endcap} \tag{21}$$

$$V_{term} = \pi r_{term}^2 h_{term} \tag{22}$$

Finally, by multiplying with the density ρ_i the mass m_i of every individual material i is known from Eq. (23). Raw densities and particle densities assumed are listed in Table 2. Detailed breakdown of all masses is necessary in order to calculate the material cost with best possible accuracy.

$$m_i = V_i \rho_i \tag{23}$$

3.3. Process model

This section introduces the models established for the processes necessary to produce a tabless cylindrical lithium-ion cell as modeled with the geometrical formulas. This is explained in the same order and categorization as visualized in Fig. 1, starting with manufacturing of the tabless jelly roll and manufacturing of the housing followed by tabless cell assembly and finishing. All monetary values are given in $. In case the sources reported values in EUR, they were converted to $ with the average exchange rate during the assumed period of time.

Table 1
Geometrical model of large-format tabless cylindrical lithium-ion cells as a function of cell dimensions and housing material, adopted from [9].

Value	Formula	
Layer trajectory	$r = a\varphi$	(1)
Constant a	$a = \frac{t_{layer}}{2\pi}$	(2)
Layer thickness	$t_{layer} = \sum t_i = 2t_{ano} + t_{cu} + t_{sep} + 2t_{ca} + t_{al} + t_{sep}$	(3)
Length of spiral curve	$\Delta S(\varphi_1, \varphi_2) = \int_{\varphi_1}^{\varphi_2} \|\|f'(\varphi)\|\|_2 d\varphi = \frac{a}{2}[\varphi\sqrt{1+\varphi^2} + \ln\left(\varphi + \sqrt{1+\varphi^2}\right)]\Big\|_{\varphi_1}^{\varphi_2}$	(4)
Inner jelly roll start angle	$\varphi_{start} = \frac{r_{start}}{a} = 2\pi(\frac{r_{core}}{t_{layer}} + \frac{1}{2})$	(5)
Outer jelly roll end angle	$\varphi_{end} = \frac{r_{end}}{a} = 2\pi(\frac{r_{cell} - t_{wall}}{t_{layer}} - \frac{1}{2})$	(6)
Core diameter	$d_{core} = 3.75\ \text{mm} + \frac{1}{20}(d_{cell} - 21\ \text{mm})$	(7)
Housing wall thickness	$t_{wall,steel} = 0.25\ \text{mm} + 0.01\ (d_{cell} - 21\ \text{mm})$	(8)
	$t_{wall,al} = 0.425\ \text{mm} + 0.015\ (d_{cell} - 21\ \text{mm})$	(9)
Coating height	$h_{coat} = h_{cell} - h_{inact,ano} - h_{inact,ca}$	(10)
Inactive height	$h_{inact,ano} = 5.5\ \text{mm}$	(11)
	$h_{inact,ca} = 4.5\ \text{mm}$	(12)
Cell energy	$E_{cell} = \Delta S(\varphi_{start}, \varphi_{end}) t_{layer} h_{coat} e_{vol,act}$	(13)

Table 2
Material densities for parameterization of the geometrical model.

Cell component	Material	Raw density in g cm^{-3}	Particle density in g cm^{-3}	Source
Housing	Al-3003	2.73	–	[44]
	Steel	7.75	–	[45]
Anode	Copper foil	8.92	–	[46]
	Graphite	–	2.25	[19]
	SiO	–	2.13	[19]
	CMC	–	1.00	[47]
	SBR	–	0.98	[48]
	Carbon black	–	1.90	[49]
	CNT	–	1.74	[50]
Cathode	Aluminum foil	2.70	–	[51]
	NMC811	–	4.78	[19]
	PVDF	–	1.92	[52]
Separator	PE	–	0.962	[53]
	Al_2O_3 coating	–	3.9	[54]
Electrolyte	DMC	1.07	–	[55]
	EC	1.32	–	[56]
	EMC	1.01	–	[57]
	FEC	1.49	–	[58]
	VC	1.40	–	[59]

3.3.1. A1) Tabless jelly roll manufacturing

The initial steps of mixing, coating, drying, NMP recovery, calendering, cutting and vacuum drying are unaffected by the tabless electrode design assuming the 90° collector plate welding technique as explained earlier. The parameterization of these steps is mainly based on existing literature with additional assumptions and can be found in the Appendix. Modeling and parameterization of the tabless winding and collector plate laser welding as a function of cell dimensions has not been reported in the literature to the best of our knowledge and is explained in the following sections.

Tabless winding

General values for the winding machine are taken from [20]. The winding time as a function of electrode length is not yet documented in public literature and based on experience from Fraunhofer Institute for Manufacturing Engineering and Automation IPA. The winding time in this study is defined as the total time of positioning and fixating the electrode separator stack within the winding machine, the actual winding process and the ejection of a wound jelly roll. The winding time itself scales in an almost linear relation to the jelly roll length considering acceleration and deceleration. Fixating and ejection are near constant offsets for a single jelly roll independent of dimensions. For instance, winding time for 1 m of jelly roll is 1.25 s while winding time for 2 m of jelly roll is 1.50 s. An increase of 100% in length increases winding time by only 20% in this example. Complete parameterization of tabless winding is summarized in Table 3 and a complete graph of winding time vs. jelly roll length is included in the Appendix.

Table 3
Parameterization of the PBCM for tabless winding per machine.

Parameter	Value	Source
Workers per shift	1	[20]
Power consumption in kW	8	[20]
Invest in mio. $	1.416	[20]
Tabless winding time in s	Appendix	This study
Scrapp loss in %	0.6	[20]
Machine area in m^2	12	[20]

Laser welding of collector plates

The following calculations for the welding steps involved in tabless cylindrical cell manufacturing have been conducted in conjunction with the Institute for Welding and Joining (ISF), RWTH Aachen University and Fraunhofer Institute for Manufacturing Engineering and Automation IPA.

The welding of the collector plates to the tabless jelly roll is visualized in Fig. 2(a). The aluminum and copper collector plates are joined with the 90° technique to the respective metal foils at the end of the jelly roll. This welding connection is similar to an overlap joint. Based on the literature it is possible to estimate welding power and speed with sufficient accuracy without the necessity of executing extensive experimental studies. However, there are many different laser types and strategies that are generally suitable to achieve the desired welding connection, such as short pulse laser welding [60,61] using a green [62]

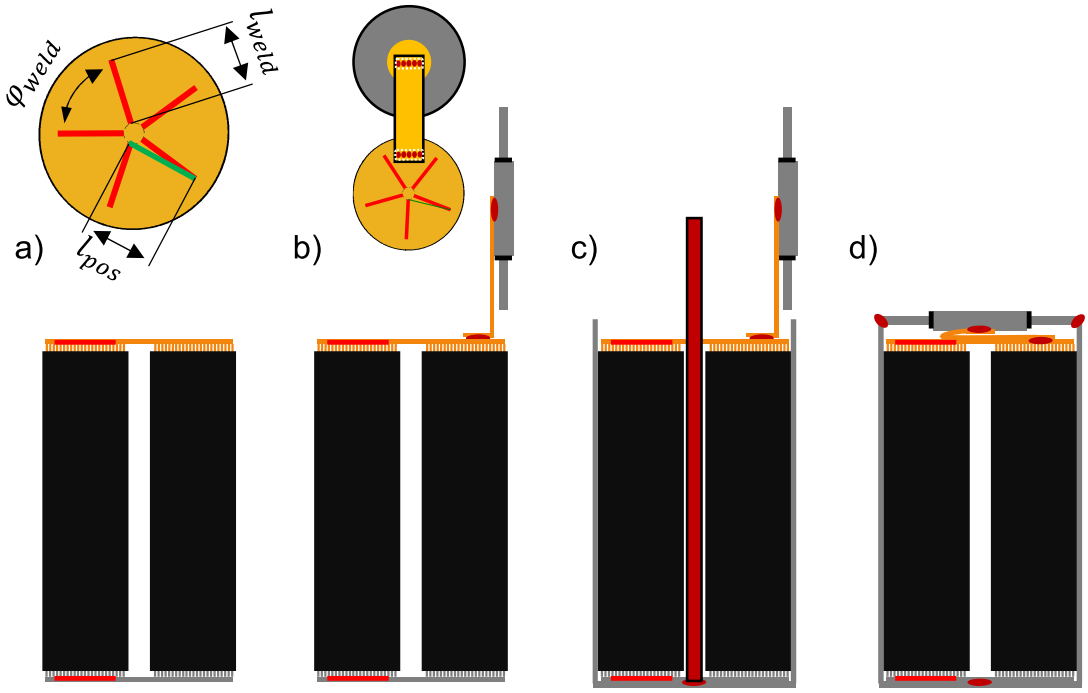

Fig. 2. Welding strategy for manufacturing a tabless cylindrical lithium-ion cell based on the reference design [7,9,27,29] with impact extruded aluminum housing and laser welded endcap. Welds are marked as red lines and dots. (a) laser welding of collector plate to the jelly roll with continuous foil overhangs in a 90° angle at the example of the anode copper collector plate. The process is identical for the cathode aluminum collector plate on the opposite side. Note that the depicted collector plate is a simplified representation without holes and grooves that are actually present within the reference cell. (b) laser welding of copper strip to collector plate and central terminal to connect the anode to the negative terminal. (c) insertion of electrode through hollow core and ultrasonic welding of aluminum collector plate to the cell bottom to connect the cathode to the positive can, (d) bending of metal strip and laser welding of endcap to can. Note that the material combinations at the weld spots would be different for cells with steel housing as the potentials of terminal and can would be reversed.

or infrared laser [63]. Using an ultra short pulse laser makes the weld seam small and thin with less heat input than continuous wave (CW) laser welding, due to the short interaction between laser and material. Disadvantageous is the rough weld seam surface and spatters on the top of the copper surface as shown in [60]. Small spatters and welding edges can lead to small voltage flashovers which can damage the cell. Additionally, the weld seam width is small with large ohmic resistance for current flow. Strategies like welding several lines with a minimal distance between each other is possible. However, the cross section of those weld seams show pores and a rough welding surface [64]. Also negative, the high investment cost is detrimental for a pulse laser compared to the CW laser. More promising are green laser which have a higher surface absorbance for copper and aluminum compared to typical NdYAG-Laser due to the smaller wavelength. Thereby, less laser power is needed to melt the material. This advantage over the infrared laser is irrelevant when getting into the deep penetration welding. In deep penetration welding, the laser beam propagates into the keyhole with multi reflection which increases the absorbance. To overcome the intensity threshold on the surface of the material to deep penetration welding, the laser source needs high beam quality and a resulting small beam diameter. This is possible with a single mode fiber laser. Additional advantage of infrared laser compared to green laser is the reduced influence of shielding gas and metal vapor on weld seam quality and stability [65]. [63] proofs the use CW fiber laser for solid overlap connection between copper and stainless steel. Therefore, a laser welding setup with CW single-mode fiber laser and programmable focus optic (PFO) is assumed for welding the collector plates to the metal foils. Additionally, a clamping device is needed to ensure exact positioning and clamping force. Miss alignments or gaps can lead to welding defects and follows with insufficient connection. A detailed description of all components assumed is supplied in the Appendix.

The welds are assumed to be distributed in a star like pattern as shown in Fig. 2(a). This represents how they are aligned in the reference cell. With the assumption of equidistant angles between the welds φ_{weld} calculates according to Eq. (24) with n_{weld} as the number of welds. Note that varying the angles between individual welds is a valid strategy to make room for larger metal connectors, but this is disregarded in this study.

$$\varphi_{weld} = \frac{2\pi}{n_{weld}} \tag{24}$$

The weld seam length l_{weld} is calculated according to Eq. (25) with k_{weld} as the weld length factor. k_{weld} determines the ratio between collector plate radius and weld length and is assumed as 0.6. Welding is executed from inside to outside in order to avoid heat collection.

$$l_{weld} = k_{weld} r_{cell} \tag{25}$$

The inner radius on the weld $r_{weld,start}$ is calculated such that the weld is positioned with the same distance to the inner and outer radius of the collector plate according to Eq. (26).

$$r_{weld,start} = r_{core} + \frac{r_{cell} - t_{wall} - r_{core} - l_{weld}}{2} \tag{26}$$

The distance for repositioning the laser l_{pos} between the end coordinates $\vec{x}_{end,i}$ of weld i and the start coordinate $\vec{x}_{start,i+1}$ of weld $i+1$ is obtained according to Eq. (27).

$$l_{pos} = norm(\vec{x}_{end,i} - \vec{x}_{start,i+1}) \tag{27}$$

The total welding time t_{weld} and positioning time t_{pos} are calculated according to Eqs. (28) and (29) with the welding speed and positioning speed v_{weld} and v_{pos}, respectively.

$$t_{weld} = n_{weld} \frac{l_{weld}}{v_{weld}} \tag{28}$$

Table 4
Parameterization of the PBCM for collector plate laser welding. The values are based on the experience of the authors unless stated otherwise.

Parameter	Value	Source
Workers per shift	0	This study
Power consumption in kW	3.01	This study
Invest in mio. $	0.451	This study
Positioning speed laser in mm s^{-1}	3000	This study
Welding speed laser in mm s^{-1}	500	This study
Clamping duration per cell in s	1	This study
Cycle time in s	Eq. (30)	This study
Machine area in m^2	2.3	[20]

$$t_{pos} = (n_{weld} - 1)\frac{l_{pos}}{v_{pos}} \tag{29}$$

The total cycle time t_{cycle} for welding the collector plates of a single cell is defined according to Eq. (30) with the clamping time t_{clamp}.

$$t_{cycle} = t_{weld} + t_{pos} + t_{clamp} \tag{30}$$

A laser power of 600 W at a welding speed v_{weld} = 500 mm s^{-1} reaches a sufficient weld penetration through a 240 µm copper foil [63] which is close to the collector plate thickness of the reference cell. For the aluminum collector plate, the same welding speed is assumed but less laser power is needed due to the lower melting point of aluminum. The welding process including the positioning of the laser beam is calculated to be 9 ms for each collector plate on cells with 18 mm diameter. An increase to 50 mm diameter increases the total welding time to 24 ms. The positioning, clamping and removing of the collector plates to the jelly roll for the welding process is estimated to be 1 s independent of the cell dimensions. Complete parameterization for collector plate laser welding is summarized in Table 4.

3.3.2. A2) Housing manufacturing

To the best of our knowledge, parameterization for manufacturing of cylindrical cell housings with different materials and manufacturing techniques as a function of cell dimensions has not been documented in the literature before. The following parameterization of a manufacturing line for cylindrical cell housing is based on the experience of industry experts from SFT-Consulting (Meisenberg, Germany).

Multistep deep drawing of steel can

Parameterization of the deep drawing process is based on values for existing real manufacturing lines for 2170 and 4680 steel cans. A 2170 line that produces 100 mio. cans requires 2.25 workers per shift, 4.13 mio. $ invest and 330 m^2 plant area, whereas a line for 4680 cans requires 4.8 workers per shift, 30.68 mio. $ invest and 825 m^2 plant area. Labor, invest and plant area are scaled by linear approximation as a function of the cell diameter. Cost of energy is assumed as 3% of the cost of material and labor [22]. Scrap loss of housing material is assumed as 6% due to the necessity of cutting off some of the deformed can material at the end of the deep drawing process. In stable state of manufacturing a variable scrap loss of 3% of housings is assumed. Complete parameterization for deep drawing of steel cans is summarized in Table 5.

Backwards impact extrusion of aluminum can

For the backwards impact extrusion process the parameterization is based on real values for a 4680 manufacturing line independent of the cell dimensions. Every cell format may be produced on the same machine by changing the dimensions of die and stamp. A manufacturing line for 80 mio pieces requires 6 workers per shifts, 11.8 mio. $ invest and 440 m^2 plant area. Scrap losses of material and housings as well as cost of energy are assumed equal to the deep drawing process. Note that in theory for cells with smaller diameter a smaller extrusion machine could be feasible. This study assumes the size of a 4680 extrusion line for all cell dimensions as no extrusion line for aluminum cells with diameter less than 46 mm is known to the authors. Complete parameterization for backwards impact extrusion of aluminum cans is summarized in Table 6.

Table 5
Parameterization of the PBCM for deep drawing of steel cans. The values are based on the experience of the authors unless stated otherwise.

Parameter	Value	Source
Workers per shift	0.1 $\frac{d_{cell}}{mm}$ + 0.11	This study
Energy cost in $	3% of cost of material and labor	[22]
Invest in mio. $	1.062 $\frac{d_{cell}}{mm}$ - 18.172	This study
Process rate in mio. pieces $year^{-1}$	100	This study
Material loss per piece in %	6.5	This study
Scrap loss in %	3	This study
Machine area in m^2	19.8 $\frac{d_{cell}}{mm}$ - 85.8	This study

Table 6
Parameterization of the PBCM for backwards impact extrusion of aluminum cans. The values are based on the experience of the authors unless stated otherwise.

Parameter	Value	Source
Workers per shift	6	This study
Energy cost in $	3% of cost of material and labor	[22]
Invest in mio. $	11.8	This study
Process rate in mio. pieces $year^{-1}$	80	This study
Material loss per piece in %	6.5	This study
Scrap loss in %	3	This study
Machine area in m^2	440	This study

3.3.3. B) Assembly

Parameterization for the manufacturing steps of tabless welding which to the best of our knowledge have not been reported in the literature are explained in the following sections. Parameterization for electrolyte filling and closing of the fill hole are supplied in the Appendix.

Laser welding of copper connector to copper collector plate and terminal

The welding process of the copper connector to the collector plate on one side and the terminal on the other side is depicted in Fig. 2(b). Proper welds for these connection can be achieved with a laser system and welding parameters of the same design and kind as for welding the collector plates to the metal foils. A small distinction in laser power for aluminum and steel housing will ensure sufficient welding penetration for both material combinations. More difficult is the positioning, clamping and integration in the assembly line. The collector plate and the housing is electrically connected via the metal connector which is a thin rectangular sheet as shown in Fig. 2(b). This thin foil can bend or break due to the desired short cycle times and the resulting acceleration force. The cycle time for contacting the terminal can be calculated similar to the contacting the collector plates. It should be noted that the contacting of the connector to the collector plate and endcap involves only two parallel welds each, the length of which is about 15% of the cell radius. Following, the positioning and clamping time are most essential on the cycle time. Complete parameterization for laser welding of copper connector the collector plate and housing is summarized in Table 7. No staff is required for laser welding.

Ultrasonic welding of aluminum collector plate to aluminum housing

After inserting the jelly roll into the can (Appendix), a short ultrasonic welding process can be used to join the aluminum collector plate to the cell bottom as depicted in Fig. 2(c). The two-in-one process step safes cycle time and is adjustable for different weld diameters. The cycle time of the contacting is estimated to be 1 s, with the actual welding process taking only 250 ms at an energy input of 80 J. Ultrasonic welding is a fully automated process, which requires no staff to operate

Table 7
Parameterization of the PBCM for laser welding of connector to cu collector plate and terminal. The values are based on the experience of the authors unless stated otherwise.

Parameter	Value	Source
Workers per shift	0	This study
Power consumption aluminum in kW	3.01	This study
Power consumption steel in kW	2.86	This study
Invest in mio. $	0.451	This study
Positioning speed laser in mm s^{-1}	3000	This study
Welding speed laser in mm s^{-1}	500	This study
Clamping duration in s $piece^{-1}$	1	This study
Cycle time in s	Eq. (30)	This study
Machine area in m^2	2.3	[20]

Table 8
Parameterization of the PBCM for ultrasonic welding of aluminum collector plate to cell bottom. The values are based on the experience of the authors unless stated otherwise.

Parameter	Value	Source
Workers per shift	0	This study
Power consumption in kW	0.52	[22]
Invest in mio. $	0.041	This study
Cycle time in s	1.0	This study
Machine area in m^2	2.3	[20]

Table 9
Parameterization of the PBCM for laser welding of the endcap to the can. The values are based on the experience of the authors unless stated otherwise.

Parameter	Value	Source
Workers per shift	0	This study
Power consumption aluminum in kW	3.01	This study
Power consumption steel in kW	2.86	This study
Invest in mio. $	0.451	This study
Welding speed laser in mm s^{-1}	400	This study
Clamping duration per cell in s	1	This study
Cycle time in s	Eq. (30)	This study
Machine area in m^2	2.3	[20]

and allows for efficient process monitoring to predict insufficient weld connections [66]. Complete parameterization for ultrasonic welding of aluminum collector plate to aluminum housing is summarized in Table 8. Note that the material combination for this weld would be copper and steel for a steel housing as the potential on the can would be reversed. The parameterization is assumed identical for both material combinations in this case as the influence on the results is expected to be negligible.

Laser welding of endcap

For welding the endcap to the can as depicted in Fig. 2 (d) a different welding setup is needed. To overcome the corner connection and generate a round weld seam, a bigger focus diameter of the laser beam is needed which can be realized in general with multimode lasers or with beam oscillation. Newer laser applications such as dynamic beam shaping [67] or multi focus such as BrightLineWeld [68] allow similar or better weld seams at higher welding speed. The best suited laser beam source for this application can only be found out by a comparative study. In our case, we refer to an adjustable ring mode laser which allows solid corner connection at 100 mm s^{-1} [69]. Laser power is estimated as 1000 kW based on an average thickness of the can. The welding speed is slower compared to the previous welding steps in order to ensure a tightly sealed cell which is a crucial quality and safety requirement. In order to precisely weld the endcap to the aluminum can, again a clamping device is needed. Same as before a clamping time of 1 s is assumed. The cycle time for sealing the housing can be calculated using Eq. (30). The length of the weld seam equals the circumference of the cell. The positioning time is omitted in this case, since the start and end points of the weld seam coincide. Complete parameterization of endcap laser welding is summarized in Table 9.

Table 10
Operating conditions for parameterization of the operations model.

Parameter	Value	Source
Location of gigafactory	Germany	[70]
Annual output in GWh $year^{-1}$	40	[70]
Shifts per working day	3	[71]
Working hours per shift	8	[71]
Working days per year	300	[71]
Machine availability in %	90	[20]

Table 11
Material prices for parameterization of the financial model.

Component	Material	Price	Unit	Year	Source
Housing	Al-3003	3.19	$ kg^{-1}	2021	SFT-Consulting
	Steel (nickel-plated)	3.54	$ kg^{-1}	2021	SFT-Consulting
Anode	Copper foil	1.20	$ m^{-2}	2022	[72]
	Copper	9.46	$ kg^{-1}	2021	[73]
	Graphite	10.0	$ kg^{-1}	2022	[72]
	C-SiO_x	25.0	$ kg^{-1}	2018	[74]
	CMC	10.0	$ kg^{-1}	2021	Manufacturer
	SBR	10.0	$ kg^{-1}	2021	Manufacturer
Anode and Cathode	Carbon black	7.0	$ kg^{-1}	2022	[72]
	CNT	90.0	$ kg^{-1}	2018	[75]
Cathode	Aluminum foil	0.20	$ m^{-2}	2022	[72]
	Aluminum	2.56	$ kg^{-1}	2021	[73]
	NMC811	26.0	$ kg^{-1}	2022	[72]
	PVDF	15.0	$ kg^{-1}	2022	[72]
Separator	Polyethylene (PE)	0.60	$ m^{-2}	2018	[74]
	Al_2O_3 coating	0.30	$ m^{-2}	2018	[74]
Electrolyte	$LiPF_6$ in EC:EMC	10.0	$ l^{-1}	2022	[72]
Solvent	NMP	2.70	$ kg^{-1}	2018	[74]

3.4. Operations model

Based on the input from the process model the resources required for producing a targeted annual output are calculated by the operations model. The operating conditions are listed in the main text. All further parameterization and formulas used in the operations model are supplied in the Appendix.

In march 2021 Volkswagen AG announced six gigafactories within Europe with an annual output of 40 GWh each [70]. Based on this the same annual output of 40 GWh produced within a gigafactory located in Germany is assumed in this study. A three-shift work day with eight working hours per shift at 300 working days per year and a machine availability of 90% is assumed as listed in Table 10.

3.5. Financial model

Based on the input from the business model the material and manufacturing cost are calculated by the financial model. The assumed material prices have major influence on the total cost and are therefore included in the main text. Further explanation of all formulas used for the financial model and values for parameterization can be found in the Appendix. Price parameterization regarding labor, capital, energy and area are based on average values of the year 2021. This period of time was chose for two reasons: (1) the prices especially for energy were inflated throughout 2022 and parts of 2023 due to the special global circumstances of this year and evaluated as not representative and (2) the access to studies and analysis for lithium-ion cell manufacturing as well as official statistical price databases was important for parameterization and validation of the model. For 2021 a large number of studies and databases were found which were not yet available for 2023 at the time of conducting this study. The parameterization of the financial model regarding material prices is therefore also mainly based on public sources from 2021 [73] and the BatPac v5.0 release from July 2022 [72]. A few values were taken from slightly older sources from 2018 [74,75]. All values that were initially given in EUR were converted to $ with an average exchange rate of 1.18 $ EUR^{-1} for the

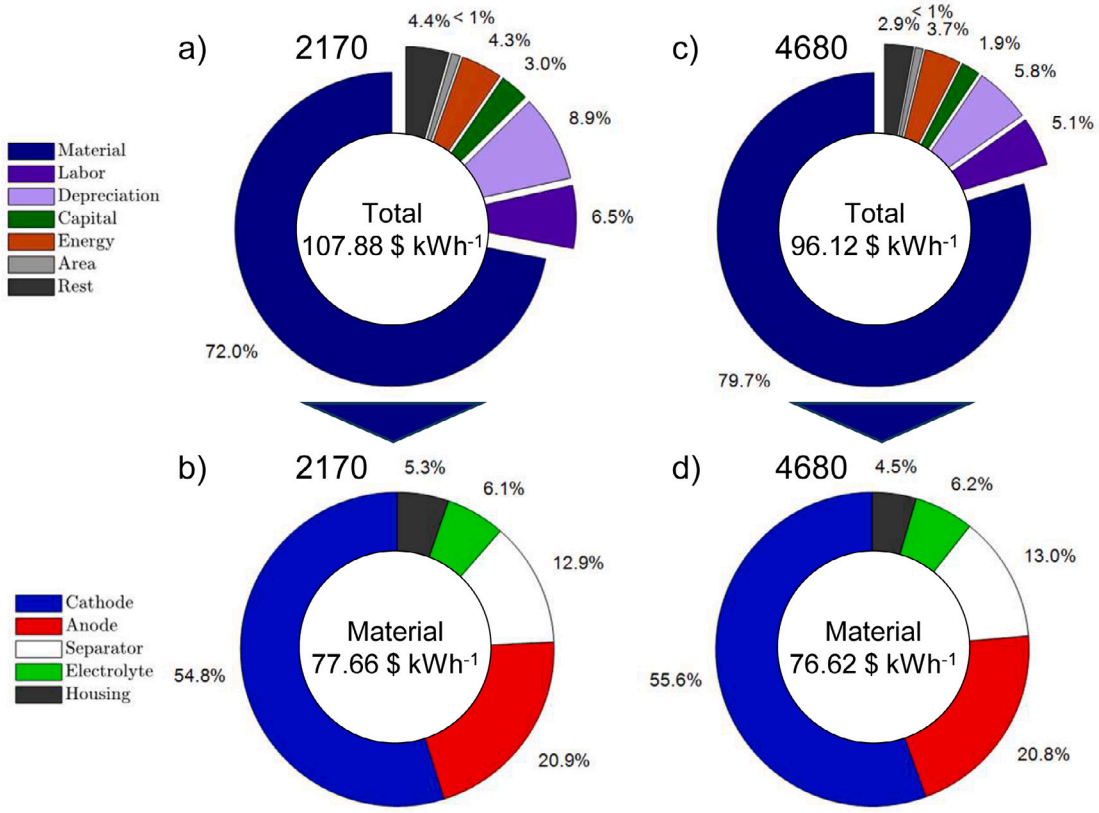

Fig. 3. In-detail breakdown of total cost. Parameterization of material prices are mainly based on values from 2021 (Table 11 and the Appendix). Top row: total cost divided into type of cost and bottom row: material cost divided into cell components for 2170 and 4680 cells with steel housing.

year 2021 [76]. Table 11 summarizes the material prices assumed in this study, the respective years and sources of the values. Prices include discounts due to the huge purchasing quantity related to the assumed annual output. Values that were taken from non-public sources include prices for CMC and SBR that were supplied by a manufacturer who wished to remain unnamed. Values for Al-3003 and nickel-plated steel were supplied by SFT-Consulting.

4. Results and discussion

This section explores the influence of cell dimensions and housing materials on the total cost. First, an in-detail comparison between the 2170 and the newly introduced large-format 4680 with steel housing is presented to establish an overall understanding of how the cost structure looks like for different standard cell formats. The calculation results are compared to the literature and public sources to verify the meaningfulness of the results. Then, the overall sensitivities of the manufacturing cost on the cell diameter, the cell height and the housing material are analyzed.

4.1. Validation

4.1.1. Exemplary cost breakdown: 2170 vs. 4680

2170

Fig. 3 shows an in-detail breakdown of the manufacturing cost of a 2170 compared to 4680 cell. Fig. 3(a) shows a donut chart divided into cost of material, labor, depreciation, capital, energy, plant area and others for a 2170 cell. An annual output of 40 GWh requires 2,540,650,000 2170 cells with an energy content of 15.74 Wh cell^{-1}. This translates to total cost of 1.70 $ cell^{-1} or 107.88 $ kWh^{-1}. The material cost has a share of 72.0% and manufacturing cost therefore has a share of 28.0%. Fig. 3(b) shows a further breakdown of the material cost. The main cost drivers are the electrode materials with the NMC cathode having the main share of 54.8% and the SiO_x-C anode having a share of 20.9%. The separator has a share of 12.9%, the electrolyte has a share of 6.1% and the steel housing has a share of 5.3%.

A recent study of Fraunhofer Institute for Systems and Innovations Research ISI analyzed the manufacturing and materials cost for different cell formats [77]. They reported average total cost of 100 EUR kWh^{-1} which equals 118 $ kWh^{-1} based on material prices, energy cost and average exchange rate of 2021 across all cell formats. The authors further state that cylindrical cells are cheapest to produce followed by prismatic cells while pouch cells are most expensive. This agrees well with the total cost of 107.88 $ kWh^{-1} calculated for the 2170 cells found in this study. It is as expected within the reported range but slightly lower than the average value across all cell formats. Further, [77] reports average manufacturing cost share of 20%–35% and average material cost share of 65%–80% across all cell formats based on extensive literature survey. The values of 28.0% for manufacturing cost share and of 72.0% for material cost share calculated in this study lay well within this range.

[77] further reports in-detail manufacturing cost breakdown at the example of a 2170 cell for manufacturing cost. They report the main manufacturing cost drivers are machine depreciation, followed by labor and energy cost. The same order is calculated by the model in Fig. 3 for the 2170 cell assumed in this study.

A study by strategic research provider BloombergNEF [78] reported average cell cost of 110 $ kWh^{-1} for NMC811 cells at the end of 2021. Again, without mentioning the specific cell format. This value agrees well with the values calculated in this study though it is slightly lower than what is reported in [77].

Overall, at the time of writing the absolute values for the total cost as well as the relative shares of manufacturing cost and material cost lay well within what is reported by other sources for the assumed

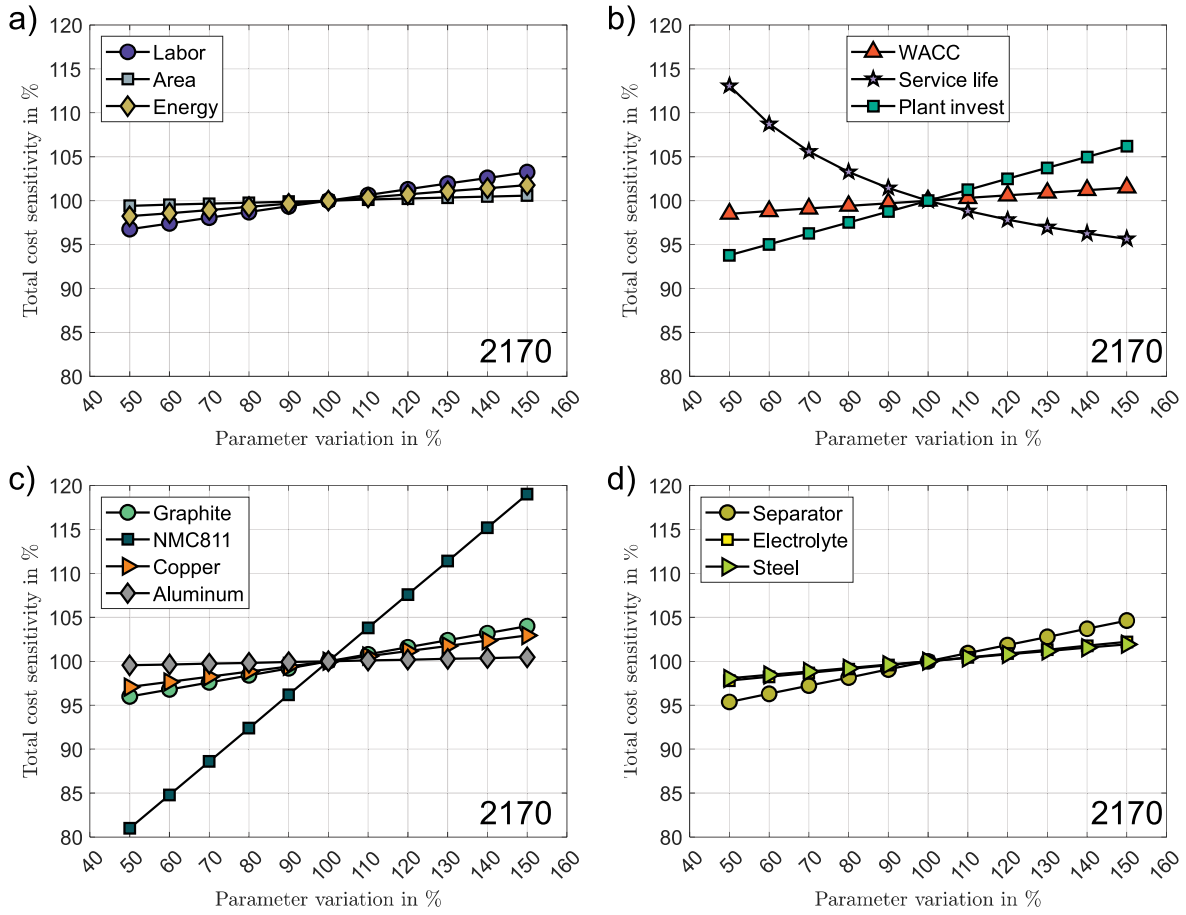

Fig. 4. Uncertainty analysis at the example of a 2170 cell with steel housing. Sensitivity of the total cost as a function of the percentage uncertainty for (a) labor, plant area and energy, (b) Weighted Average Cost of Capital (WACC, detailed explanation in the Appendix), service life and plant invest, (c) price of graphite, NMC811, copper and aluminum, (d) price of separator, electrolyte and steel. An especially strong sensitivity of the total cost on the price of cathode material is identified.

period of time. We emphasize that material prices vary on a daily basis and various different manufacturing technologies are used by different manufacturers. Thus, the model presented in this study is suitable to analyze absolute values only for the assumed period of time. However, we emphasize that this study focuses on revealing the influence of varying diameter, height and housing material. The overarching influence of those variables on the total cost is expected to be largely independent of raw material prices. We thus conclude that the absolute values from this study are valid only for price parameterization within the assumed period of time. The qualitative relationships with regard to the variables investigated however are expected to remain valid even if material prices and boundary conditions change in the future.

4680

In contrast, Fig. 3(c) and (d) show the same cost breakdowns for the 4680 cell. In this case, for the annual output of 40 GWh only 431,170,000 4680 cells with an energy content of 92.77 Wh cell^{-1} are required compared to the 2,540,650,000 2170 cells. This equals 8.92 $ cell^{-1} or 96.12 $ kWh^{-1} which is a reduction of 10.9% compared to 107.88 $ kWh^{-1} for the 2170. The material cost now has a share of 79.7% compared to the of 72.0% of the 2170. This is mainly caused by significantly lower manufacturing cost and less so by a change in material cost. The material cost in Fig. 3 (d) decreases slightly to 76.62 $ kWh^{-1} compared to 77.66 $ kWh^{-1} for the 2170. The underlying reasons for these observations will be analyzed in detail within the following sections.

Overall, a total cost decreases for the 4680 cell compared to the 2170 cell was expected as this was one of the reasons Tesla introduced the 4680 as was publicly stated [1]. The cost decrease mainly arises from lower cost of manufacturing while material cost varies only slightly. This was already hypothesized by Quinn et al. [24] and Waldmann et al. [25] and is confirmed here. Thus, we overall conclude the general influence of varying dimensions agrees with what would be expected based on scientific literature and non-scientific public sources.

4.1.2. Uncertainty analysis

Fig. 4 shows the sensitivity of the total cost on different parameters for 2170 cells with steel housing and assumed 40 GWh annual output. The x-axis shows the percentage variation of a single parameter and the y-axis shows the resulting impact on the total cost with respect to the 2170 baseline scenario. For cost of labor, area and energy in Fig. 4(a), a positive linear correlation for all parameters is visible with rather low sensitivity. Even an extreme variation of 50% for one of these parameters results in less than 4.5% change in total cost. For WACC and invest in Fig. 4(b) a similar positive correlation exists, however the latter has a larger influence on the total cost. An uncertainty of 50% results in 6.2% change of total cost. The service life of machinery has a strong and nonlinear degressive influence on the total cost. This is because the depreciation is calculated as the quotient between invest and service life. Cutting the service life in half results in 13.1% larger total cost, while extending the service life by 50% results in 4.3% less total cost. The influence of the material cost in Fig. 4(c) and (d) all have a positive and linear correlation to the manufacturing cost. An uncertainty in the price of graphite, copper, aluminum, separator material, electrolyte and steel by 50% however all have an influence of less than 5% on the total cost. The price of NMC811 has by far the greatest influence of all parameters considered. This was already

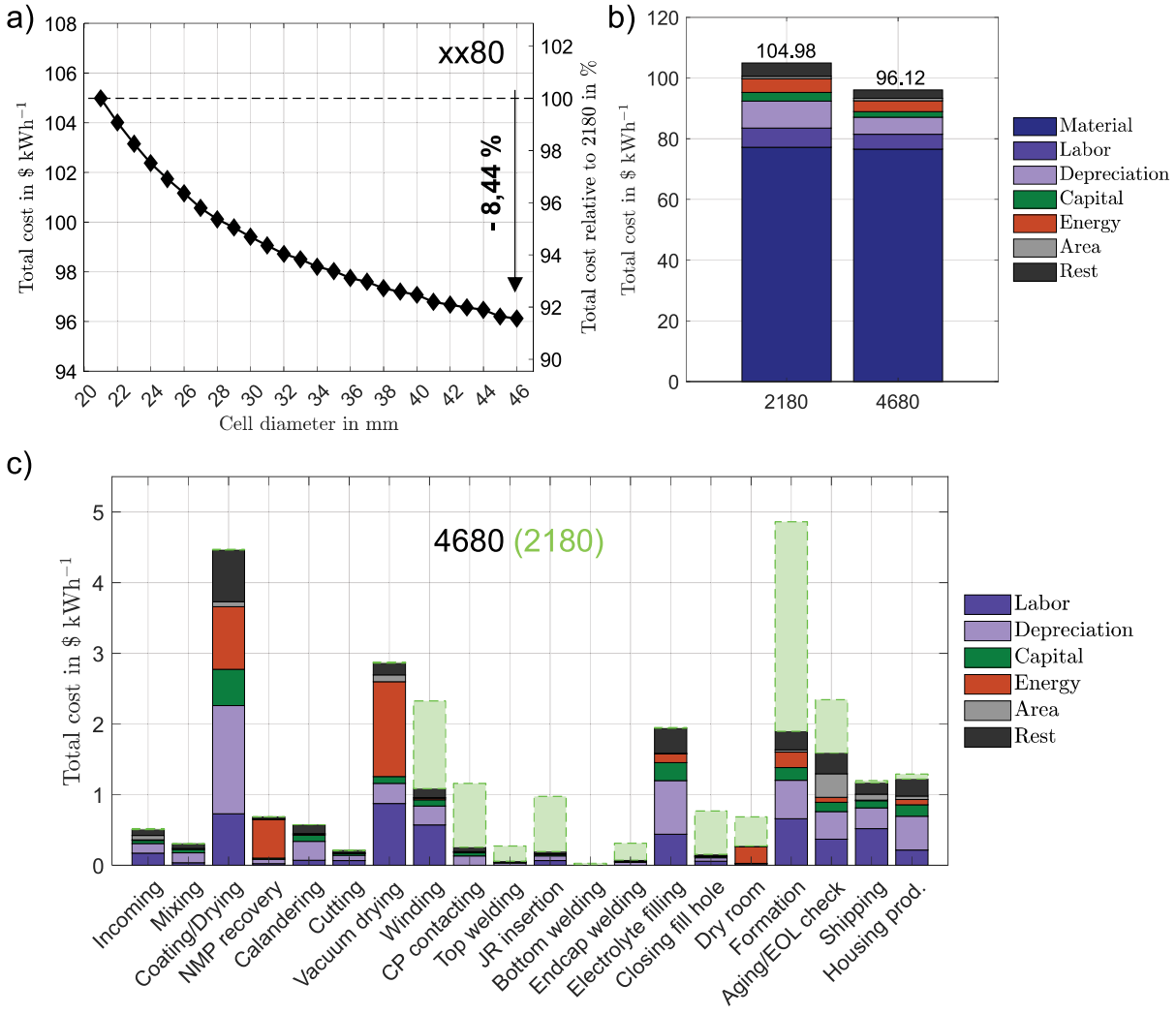

Fig. 5. Influence of the cell diameter and the manufacturing cost of tabless cylindrical lithium-ion cells with steel housing. (a) Absolute and relative manufacturing cost for varying cell diameters compared to the manufacturing cost of a 2180 cell. (b) comparison of cost breakdown between a 2180 and 4680 cell for material, labor, depreciation, capital, energy, plant area and other. (c) comparison of cost breakdown for each manufacturing step.

expected from Fig. 3(a) and (b) that show the material cost makes up 72.0% of the total cost while the cathode is responsible for 54.8% of the material cost. This means the cathode makes up 39.46% of the total cost. An uncertainty of 50% in the price of NMC811 therefore results in nearly 20% change of the total cost. Overall, there is no single parameter that has enormous influence on the total cost except for the price of NMC811. Therefore, we conclude that even if some parameters vary on daily basis and some have a degree of uncertainty due to the difficulty of accurately parameterizing a PBCM for lithium-ion cells, the model is fully applicable for understanding the influence of cell dimensions and housing materials which is the main focus of this study.

4.2. Influence of cell dimensions

4.2.1. Influence of cell diameter

Fig. 5(a) shows the total cost as a function of the cell diameter for xx80 cells with constant height of 80 mm and variable diameter between 21 mm and 46 mm. For the assumed annual output of 40 GWh 2,177,700,000 2180 cells and 431,170,000 4680 cells are required which is a reduction of 80.2%. This value is important for later analysis. For 2180 cells total cost of 104.98 $ kWh^{-1} is calculated. Enlarging the diameter decreases the total cost to 96.12 $ kWh^{-1} for 4680 cells which is a decrease of 8.44%. The curve shows a near quadratic shape. Fig. 5 shows (b) shows a cost breakdown divided by type of cost. Similar to Fig. 3(a) it is visible that the material cost is almost constant while the cost of labor, depreciation, capital, energy, area and other cost decreases. Material cost decreases only slightly from 77.18 $ kWh^{-1} to 76.62 $ kWh^{-1} while manufacturing cost decreases from 27.80 $ kWh^{-1} to 19.50 $ kWh^{-1}. Further understanding of the underlying reasons for this observation can be gained from Fig. 5(c) that shows the aforementioned types of cost for each manufacturing step for a 4680 cell in colored blocks with the overall cost for 2180 cells in one large dotted green block. In other words, the green blocks on top of the colored blocks represent the overall manufacturing cost savings for 4680 cells compared to 2170 cells. The cost for manufacturing of the electrodes up to vacuum drying is almost unchanged as these steps are performed independent of the cell diameter. During winding the first major decrease in manufacturing cost of 54% is visible. This is because with larger diameters less cells are required and less time is wasted for fixating the electrode-separator stack at the beginning of the winding process and ejecting a finished jelly roll as those are assumed constant independent of the diameter. The winding time including acceleration and deceleration is however a function of the length of the jelly roll. Therefore, the cost decrease does not scale exactly with the decrease in number of cells of 80.2%. Manufacturing cost for welding of the collector plate onto the ends of the foil overhangs decreases by 78.0%.

This is because the time required for positioning is much greater than the actual welding process itself. Positioning time is assumed as 1 s while the welding process takes 85 ms for a 2180 cell and 186 ms for a 4680. The overall process time for a single cell therefore increases very slightly while the number of cells required decreases significantly. For the same reason manufacturing cost for laser welding of the metal connector to the top collector plate and the terminal, ultrasonic welding of the bottom collector plate and laser welding of the endcap to the can decrease by 79.2%, 79.8% and 76.5%, respectively. For insertion of the jelly roll into the can a cost decrease of 80.0% is achieved which almost perfectly matches the decrease of cells required as the process time is assumed independent of the cell dimensions. An underutilization of the last machine however may lead to small deviations between both values. For electrolyte filling the cost is nearly identical as a constant volumetric filling time as in $s\ ml^{-1}$ is assumed and the required electrolyte volume is in linear relationship to the total cell capacity which is constant for a given targeted annual output. In reality, the electrolyte volumetric filling time is expected to have a dependency on the cell height as was hypothesized before [79]. We therefore recommend reviewing and updating the assumptions for this manufacturing step as a more sophisticated formula is found. Cost for closing of the fill hole also decreases by 80.0% and behaves similar to the number of cell required with small influence of underutilization of the last machine. Cost for dry room decreases by 60.2%. As only the cell assembly is conducted in the dry room, this value is dependent on the reduction of required plant area for the assembly of the 4680 cells compared to the 2170 cells. For formation, a relative cost decrease of 61.0% and the largest absolute cost reduction of 2.97 $ kWh^{-1} is achieved. The cost for formation is mainly determined by the required number of channels and control panels and to a minor degree by the cell capacity. Therefore, the decreased number of required cells significantly reduces the formation cost which is only offset by the larger cost per channel due to the increased cell capacity to a lesser degree. Cost for aging is reduced by 32.3%. These costs are partly a function of the storage area required. As the cell energy density increases with increasing diameter due to less share of inactive housing and core area, less storage area is required for the same targeted annual output. The major cost reduction however is caused by the lower amount of control panels required. One control panel is assumed to be designed to operate 50000 cells per day and therefore the required amount decreases significantly. Cost for shipping reduces only slightly as it is mainly determined by the weight and therefore the specific gravimetric cell energy density which does increase for larger cells due less share of wall thickness [9]. The cost for producing the deep drawn steel housing decreases slightly as less housings need to be produced which however is offset by larger cost for invest, labor and area. Further discussion of the cost saving potential of housing manufacturing will be done in a later section.

The manufacturing steps that are related to the tabless design assumed in this study (welding of the collector plates, contacting of the top collector plate to the terminal and contacting of bottom collector plate to the can bottom) are responsible for 0.3168 $ kWh^{-1} for a 4680 cell. This is only 1.9% of the manufacturing cost and 0.33% of the total cost. Further optimizing the tabless design therefore likely has greater impact on the thermo-electrical performance and safety features of the cell [9,29] and less so on future cost saving efforts.

In summary, a significant decrease of the manufacturing cost of 29.9% from 27.80 $ kWh^{-1} to 19.50 $ kWh^{-1} was achieved by enlarging the diameter from 2180 to 4680 and further decrease for even larger diameters is expected.

4.2.2. Influence of cell height

Fig. 6(a) shows the manufacturing cost as a function of the cell height for 46xxx cells with constant diameter of 46 mm and variable height between 80 mm and 120 mm. For achieving 40 GWh annual output 431,170,000 4680 cells are required compared to 274,380,000 46120 cells which is a decrease of 36.36%. A 46120 cell has an energy content of 145.78 Wh $cell^{-1}$ and costs 13.56 $ $cell^{-1}$ compared to the 92.77 Wh $cell^{-1}$ and 8.92 $ $cell^{-1}$ for the 4680. By enlarging the cell height from 80 mm to 120 mm, total cost decreases by 3.26% from 96.12 $ kWh^{-1} to 92.99 $ kWh^{-1}. Material cost decreases slightly from 76.62 $ kWh^{-1} to 75.62 $ kWh^{-1} while the manufacturing cost decreases by 10.92% from 19.50 $ kWh^{-1} to 17.37 $ kWh^{-1}. Fraunhofer Institute for Systems and Innovation Research ISI recently stated they expect a cost saving potential of up to 20% in manufacturing cost by increasing the cell height from 4680 to 46120 [79]. With the assumptions made in this study this seems optimistic. However, if a dry coating process would reduce or eliminate the cost of electrode manufacturing in the coating/drying, NMP recovery and vacuum drying steps that are not sensitive to the cell dimensions, the remaining manufacturing steps that are indeed highly sensitive would have a larger share and a manufacturing cost reduction of 20% or even more may become realistic based on our assumptions. The overall shape of the curve in Fig. 6(a) looks fairly linear as the cell energy has a linear relationship to the cell height according to Eqs. (10)–(12). However, from Eq. (10) the coating height and therefore cell energy is calculated by subtracting a constant inactive offset from the cell height that is required to integrate the tabless design. The larger the cell height the more the cell energy density converges against the active material energy density. Therefore, the percentage gain in cell energy is larger for cells with less height when adding a given absolute additional height [9]. For this reason the curve is not perfectly linear but flattens towards larger heights. Further, the curve oscillates up and down around certain heights. This is because the working width of electrode manufacturing machines is not always perfectly utilized. This did not have an influence for varying only the diameter in the previous section. Fig. 6(b) shows the cost breakdown of a 4680 compared to a 46120 cell. The cost reduction takes place almost exclusively within the manufacturing cost while the material cost is only slightly reduced as the ratio between dead volume and jelly roll volume decreases for larger heights. Fig. 6(c) shows the comparison of the cost breakdown for each manufacturing step between a 4680 in one large green block and a 46120 in colored blocks divided into cost types. Again, the cost of manufacturing the electrodes is nearly unchanged. The cost of winding, laser welding of the collector plates, laser welding of the top collector plate to the terminal, insertion of the jelly roll into the can, ultrasonic welding of the bottom collector plate to the can bottom, laser welding of the endcap, closing of the fill hole, Aging/EOL check and housing manufacturing all show a cost reduction between 33.47% and 37.0% and are directly correlated to the percentage decrease of required cells of 36.36%. Cost for electrolyte filling shows almost no change as the filling time is assumed as a function of the total electrolyte volume required which itself depends on the total required capacity as discussed earlier. Same as for a change in diameter, the cost of formation reduces by 27.32% which is less than the change of cells required as the number of required channels and control panels decreases accordingly but the cost per channel on the other hand increases for larger cell capacities. Cost for the dry room decreases by 22.3%. Cost for shipping is again almost constant.

Overall, it can be concluded that enlarging the cell height decreases the manufacturing cost. In this case, an increase of the cell height reduced the manufacturing cost by 10.92% from 19.50 $ kWh^{-1} to 17.37 $ kWh^{-1} and further reduction is expected for even larger heights.

4.2.3. Influence of number of cells

In the previous section the influence of the cell dimensions was analyzed and the number of cells required was identified as a major factor. Fig. 7 further deepens the understanding of the relationship between cell diameter, cell height, number of cells as well as material cost, manufacturing cost and total cost. Fig. 7(a) shows the number of cells required as a function of the cell diameter between 21 mm and as large as 60 mm with each curve representing a different cell height between 70 mm and 120 mm. As reported in [9] the volumetric energy

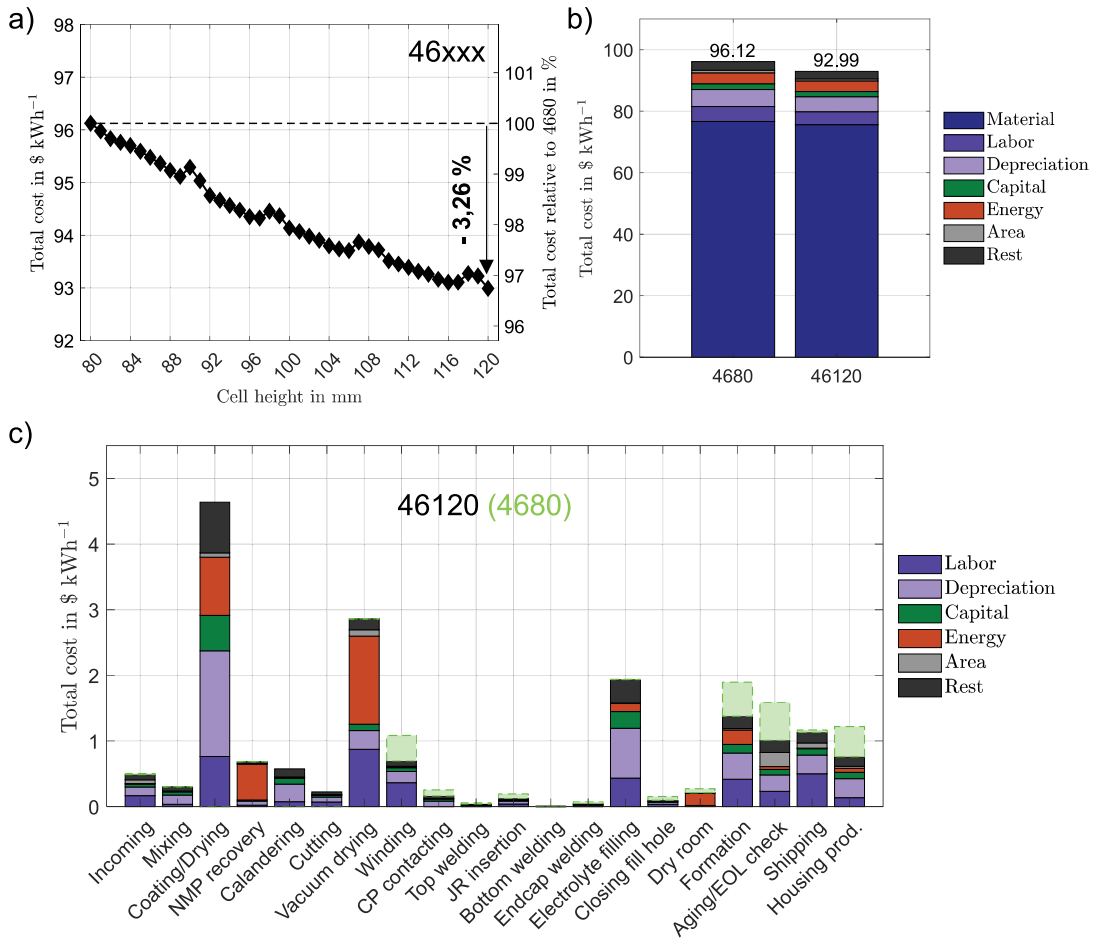

Fig. 6. Influence of the cell height on the manufacturing cost of tabless cylindrical lithium-ion cells with steel housing. (a) absolute and relative manufacturing cost for varying cell heights compared to the manufacturing cost of a 4680 cell. (b) comparison of cost breakdown between a 4680 and 46120 cell for material, labor, depreciation, capital, energy, plant area and other. (c) comparison of cost breakdown for each manufacturing step.

density increases with larger dimensions due to less areal share of inactive components. Therefore, the required number of cells decreases stronger than d_{cell}^2 for a given height. For example, the 4680 cells has 4.7982 times the cross section of a 2180 while 5.0507 times the amount of 2180 cells is required compared to 4680. The number of cells required decreases 5.3% stronger than the cell cross section for 80 mm height due to less share of housing area (Eq. (8)–Eq. (9)). This equals exactly the increase in specific volumetric energy density of the cell. The energy density also increases with the cell height due to a constant inactive offset between the cell height and the coating height of the electrodes (Eqs. (10)–(12)). Shorter cells therefore gain a larger percentage increase in energy density from a given absolute addition of height [9]. This is visible in Fig. 7(a) as the cell height shifts the number of cells required up or down but the relative reduction in required cells reduces the larger the cell for fixed steps of adding 10 mm of cell height.

Fig. 7(b) shows the material cost and total cost while the difference between both equals the manufacturing cost for the same parameter variation of diameters and heights. The total cost and manufacturing cost decreases. The material cost stays almost constant for a given height. Therefore, the percentage decrease of the total cost is weakened compared to the percentage reduction in number of cells required. This leaves the following summarizing conclusions:

- Observation: The material cost has low sensitivity on the number of cells required.
  Reason: The components of the active material are the main material cost drivers (Fig. 3) while the housing material plays a minor role. The amount of active material required scales with the annual output. If the annual output is assumed constant, the material cost for the active material remains constant.
- Observation: The manufacturing cost has a noticeable sensitivity on the number of cells required.
  Reason: Some manufacturing steps have aspects that are directly correlated to the number of cells required.
- Observation: The percentage decrease in manufacturing cost is significantly lower than the percentage decrease of the number of cells required.
  Reason: The manufacturing steps that are related to the electrode preparation are mostly unaffected by the cell dimensions and thus the number of cells required. The manufacturing steps that are indeed heavily influenced by the number of cells however also do not show a perfect linear correlation. Some cost shares are constant independent of the number of cells and some cost shares scale with the dimensions and thus weaken the relationship. Examples were given in the previous sections.

This leads to the first finalizing main conclusion of this study. There exists a cost saving potential through enlarging the cell dimensions and reducing the number of cells. It is however limited as it is almost

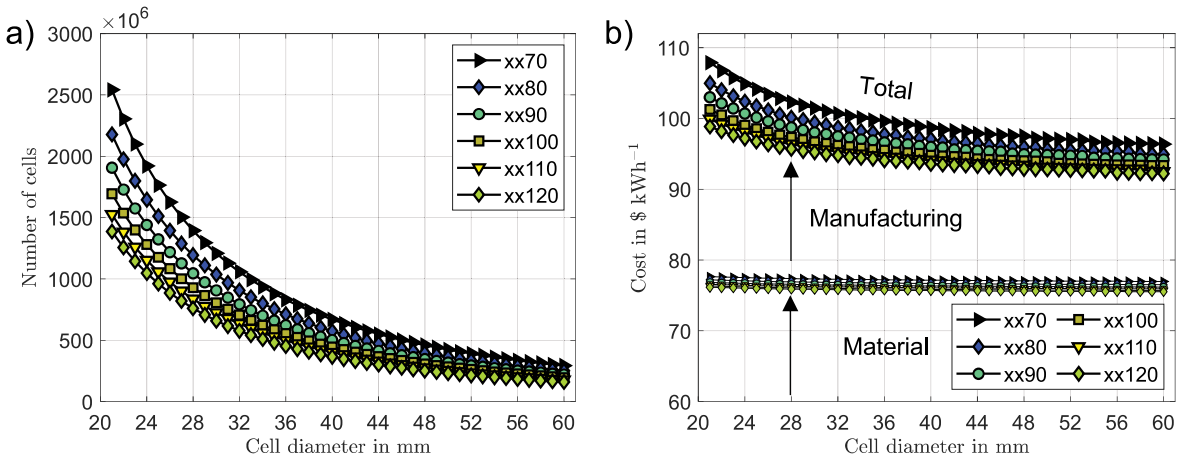

Fig. 7. Sensitivity of the manufacturing cost on the number of required cells for 40 GWh assumed annual output. (a) Number of required cells and (b) material, manufacturing and total cost as a function of cell diameter between 21 mm and 60 mm with each curve representing a cell height between 70 mm and 120 mm.

exclusively drawn from a portion of a limited number of manufacturing steps. The manufacturing cost does not decrease indefinitely but converges.

Generally, enlarging the cell dimensions is comprehensive from a cost saving perspective. With the assumptions made in this study it is likely a large portion of the cost saving potential has been realized with the switch from 21 mm diameter to 46 mm diameter. Fig. 7(b) also suggests that OEMs who have chosen the 46xxx format like BMW with their 4695 and 46120 [11] or Nio with their 46105 [80,81] have a noticeable further economic advantage over Tesla [1] and other OEMs like General Motors [82] that are rumored to adopt the 4680 format. Increasing the cell dimensions beyond the above mentioned values could be feasible to squeeze out the last bit of cost saving from these variables. Cell heights beyond 120 mm could be more beneficial from a cost saving perspective than diameters beyond 46 mm as the volumetric energy density increases stronger with the height than with the diameter [9]. Introducing extremely large cylindrical cells should however be carefully considered with respect to the thermo-electrical performance, required cooling strategies, achievable packing density and thermal propagation safety.

4.3. Influence of housing material

Fig. 8 shows a breakdown of the manufacturing cost for steel and Al-3003 housings for (a) 2170 and (b) 4680 cells. Steel housings are manufactured with a multi-steep deep drawing process while aluminum housings are manufactured with a backwards impact extrusion process. 2170 steel housings cost 5.61 $ kWh^{-1} while 4680 steel housings cost 4.67 $ kWh^{-1}. This is achieved because the material cost decreases due to less relative share of housing volume to active material volume for larger dimensions as the energy density increases with larger cell diameters and cell heights. The manufacturing cost decreases only slightly as larger machines are required that cause more depreciation while the cost for labor decreases. 2170 aluminum housings costs 6.51 $ kWh^{-1} while 4680 aluminum housings cost 2.27 $ kWh^{-1}. The relatively high manufacturing cost for extruded 2170 housings is caused as the parameterization is based on a real 4680 extrusion line that may produce very large dimensions. No data was available or known to the authors for extrusion lines specifically tuned for 2170 housings. This is an uncertainty for the manufacturing cost of 2170 aluminum housings that vanishes for larger dimensions towards the correct parameterization for 4680 cells. What is especially interesting is that the specific material cost per kWh of aluminum housings is significantly lower compared to the steel housing for all dimensions. Although required wall thicknesses of aluminum housings are about 1.6 times larger than wall thicknesses of steel housings due to less tensile strength and temperature stability of the raw material [9], material cost for 4680 aluminum housings of 1.36 $ kg^{-1} is 60.6% lower than 3.45 $ kg^{-1} for 4680 steel housings. Assumed raw material cost of 3.19 $ kg^{-1} for aluminum is similar to 3.54 $ kg^{-1} for steel. However, the density of aluminum is only 2.73 g cm^{-3} and therefore only about 1/3rd of 7.75 g cm^{-3} for steel. This results in noticeably lower housing material cost of aluminum cells for all cell dimensions compared to steel cells. The total cost of 4680 cells with steel housing was calculated to 96.12 $ kWh^{-1} (Fig. 3). For 4680 cells, impact extruded aluminum housings cost 2.27 $ kWh^{-1} while deep drawn steel housings cost 4.67 $ kWh^{-1} despite thinner walls which is an absolute difference of 2.4 $ kWh^{-1}. This is 2.5% of the initial total cost of 96.12 $ kWh^{-1} of 4680 cells with steel housing. This is an incredibly large cost saving potential from a component that has not received a lot of attention in the past. In addition, it was previously reported that aluminum housings significantly boost the thermo-electrical behavior due to larger thermal conductivity and less ohmic resistance compared to steel [9] and further allow for tighter packing density [27]. This makes the choice of housing material a crucial decision for automotive manufacturers during development that may lead to an advantage not only in performance and weight but also cost.

5. Conclusion

This study introduced a process-based cost model to analyze the influence of cell dimensions and housing material on the manufacturing and material cost of tabless cylindrical lithium-ion cells.

It was found that enlarging the cell dimensions reduces the total cost for two reasons. First, the larger the cells, the lower the manufacturing cost due to a direct dependency of certain manufacturing steps on the number of cells produced. Second, for larger dimensions the cell volumetric energy density increases due to less share of inactive components which further reduces the total cost. Overall, the material cost however remained rather constant it is mainly determined by the annual output in terms of energy content and the required active material components are the main cost drivers. Assuming an annual output of 40 GWh, increasing the cell dimensions from the conventional 2170 to the new 4680 format achieved a cost reduction from 107.88 $ kWh^{-1} to 96.12 $ kWh^{-1} or 10.9%. The overall cost saving potential of further enlarging the dimensions is however limited as it is mainly realized within only a certain number of manufacturing steps.

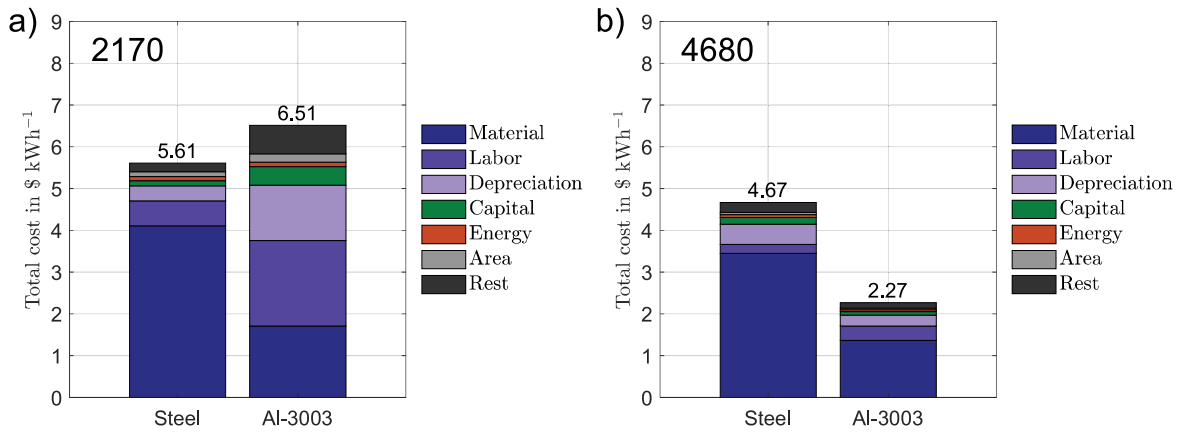

Fig. 8. Total cost for the housing as a function of cell dimensions, housing material and manufacturing technique. (a) and (b) manufacturing cost for 2170 and 4680 housings, respectively, made from deep drawn steel cans or impact extruded aluminum cans with laser welded endcaps in both cases.

The choice of housing material was identified as another opportunity to lower the cost that has not received a lot of attention in the past. Due to the better flow behavior for housings made of aluminum a backwards impact extrusion process may be applied instead of the conventional deep drawing process for nickel-plated steel housing that is highly flexible with regard to the cell height. For 4680 cells, the total cost of the housing can be reduced by 51.4% through introducing aluminum housings. This equals a cost reduction of as much as 2.5% of the total cost of 4680 cells with steel housing. A large portion of this is achieved by lower cost of the required amount of aluminum raw material compared to nickel-plated steel.

Overall, it was shown that the trend to larger cylindrical cell dimensions results in significant cost reduction and the choice of housing material should further be considered in this regard.

CRediT authorship contribution statement

Hendrik Pegel: Writing – original draft, Visualization, Validation, Supervision, Software, Resources, Project administration, Methodology, Investigation, Formal analysis, Conceptualization, Data curation. **Adrian Grimm:** Writing – original draft, Visualization, Validation, Software, Methodology, Investigation, Formal analysis, Conceptualization, Data curation. **Christian Frey:** Writing – review & editing, Validation, Methodology, Investigation. **Volker Seefeldt:** Writing – review & editing, Validation, Investigation. **Sabri Baazouzi:** Writing – review & editing, Validation, Investigation. **Dirk Uwe Sauer:** Writing – review & editing, Supervision.

Declaration of competing interest

The authors declare that they have no known competing financial interests or personal relationships that could have appeared to influence the work reported in this paper.

Data availability

The data that has been used is confidential.

Acknowledgment

The authors thank cell manufacturer BAK Battery for providing important insight and participating in valuable scientific discussion about all aspects of manufacturing for optimized battery systems with tabless cylindrical lithium-ion cells.

Symbol	Meaning	Unit
Latin		
A	Area	m^2
a	Archimedean spiral constant	m
BC	Bound capital	$
C	Capacity	Ah
CO	Cost	$
d	Diameter	m
E	Energy	Wh
$e_{vol,act}$	Volumetric active material energy density	Wh l^{-1}
h	Height	m
INV	Invest	$
IR	Interest rate	%
k_{weld}	Weld length factor	–
l	Length	m
M_{prelim}	Quantity of preliminary product per cell	–, kg, m^{-2}, l
MA	Machine availability factor	–
m	Mass	kg
n	Number, amount or quantity of components or material	–, kg, m^{-2}, l
P	Power	W
PR	Process rate	–, kg, m^{-2}, l per respective unit
p	Specific price	$ per respective unit
RW	Residual worth	$
RINV	Reinvest	$
r	Radius or radial coordinate	m
ΔS	Archimedean spiral length	m
S_p	Scrap losses	%
SL	Service life	years
t	Thickness or time	m, s
U	Voltage	V
UT_{last}	Utilization of last machine	–
V	Volume	m^3
v	Speed	m s^{-1}
WACC	Weighted average cost of capital	%
$\vec{x}$	Weld coordinate vector	m

Symbol	Meaning	Unit
Greek		
η_{CE}	Coulomb efficiency	%
η_{cell}	Energy efficiency	%
$\kappa_{electrolyte}$	Eletrolyte overfill factor	–
ρ	Density	kg m^{-3}
$\phi_{electrode}$	Electrode porosity	–
φ	Archimedean spiral angle	–
φ_{weld}	Angle between star pattern welds	–
ψ_i	Gravimetric share constant of material i	–

Subscript and superscript	Meaning
Subscripts	
act	Active material
al	Aluminum
ano	Anode
area	Machine, manufacturing or plant area
bot	Housing part can bottom
ca	Cathode
can	Housing part can
cap	Capital
cell	Cell or cells
chc	Charging
clamp	Clamping for fixation
coat	Electrode coating
core	Hollow core of cylindrical cell
cu	Copper
cycle	Cycle of a certain manufacturing step
cycler	Cycler for formation or aging
depr	Depreciation
dryer	Dryer for electrode drying
dsc	Discharging
electrode	Electrode
electrolyte	Electrolyte
end	End angle or coordinate
endcap	Housing part endcap
energy	Energy
first	First formation cycle
form	Formation
i	Material i or ith weld of star pattern
inact	Inactive height at cell ends
j	Component j of active material
lab	Labor
layer	Repetitive layer of active material
mach	Manufacturing machine or machines
maint	Maintenance
manu	Manufacturing
mat	Material
nmp	N-Methyl-2-pyrrolidon
nom	Nominal value
overh	Overhead
pores	Pores within electrode or separator
pos	Positioning
prod	Product
salable	Salable cells
scrap	Scrapped cells or preliminary product
sep	Separator
solid	Solid material share
spc	Specific value
start	Start angle or coordinate
steel	Steel (nickel-plated)
steps	Manufacturing steps
swd	Shifts per working day
target	Targeted annual output
term	Housing part terminal
tot	Total or absolute value
wall	Housing wall
wdy	Working days per year
weld	Weld or welds
wh	Working hours
whs	Working hours per shift
wm	Workers per machine
Superscripts	
i	Material i
j	Manufacturing step j
k	Running variable in product notation

Table A.12
Parameterization of the PBCM for mixing.

Parameter	Value	Source
Workers per shift	0.25	[20]
Power consumption anode in kWh	14	[20]
Power consumption cathode in kWh	19	[20]
Invest in mio. $	3.0	[20]
Mixing duration anode in min	140	[20]
Mixing duration cathode in min	270	[83]
Planetary mixer volume in l	1120	[20]
Scrap loss in %	1	[20]
Machine area in m^2	11.4	[20]

Appendix. Full parameterization of PBCM

A.1. Process model

A.1.1. A1) Tabless jelly roll manufacturing

Mixing

Machines for mixing anode and cathode are separated to prevent cross contamination. For binder solution an anchor stirrer with dissolver disc is used. Process times for mixing of the anode are taken from [20] and for NMC811 from [83]. As the bottleneck is the planetary mixer, all other machinery are designed to match the capacity thereof. Other values are taken from [20] as listed in Table A.12.

Coating and drying

A sequential coating process is assumed where one side of the metal foils is coated and dried first and afterwards the opposite side. It is assumed the power consumption can be approximated according to the formula listed in Table A.13. For the coating speed a value of 52 m min^{-1} is calculated as an average of a survey of recent literature and data from machine suppliers [20,38,72,84,85]. For the working width values of 250 mm to 1500 mm are reported in the literature for coating and drying, [20,35,72,84,85], 600 mm to 1500 mm for calendering [20,21,84,85] and 600 mm for cutting [20]. For this study, a working width of 1000 mm is assumed throughout all manufacturing steps that handle the same geometry of coated foils. Drying times for anode and cathode are a function of the gravimetric coating density as the quotient from absolute coating weight m_{coat} and electrode area $A_{electrode}$. Dryer length l_{dryer} is calculated by multiplying coating speed v_{coat} with the drying time t_{dry}.

NMP recovery

NMP recovery is exclusively necessary for cathode manufacturing as the anode uses water as solvent. Values for parameterization are taken from [20,71,72,87] as listed in Table A.14.

Table A.13
Parameterization of the PBCM for coating and drying.

Parameter	Value	Source
Workers per shift	4	[20]
Power consumption anode in kWh	350 ($\frac{l_{dryer}}{35\ \mathrm{m}}$)	[20]
Power consumption cathode in kWh	510 ($\frac{l_{dryer}}{36\ \mathrm{m}}$)	[20]
Invest in mio. $	24.55	[20]
Coating speed in m min^{-1}	52	[20,38,72,84,85]
Working width in mm	1000	[20,35,72,84,85]
Drying duration anode in s	0.25 $\frac{m_{ano}}{A_{ano}} \frac{m^2 s}{kg}$ + 2.18 s	[86]
Drying duration cathode in s	0.22 $\frac{m_{cat}}{A_{ca}} \frac{m^2 s}{kg}$ + 0.95 s	[86]
Dryer length in m	v_{coat} t_{dryer}	[20]
Machine area in m^2	3 (2 + $\frac{l_{dryer}}{m}$)	[20]

Table A.14
Parameterization of the PBCM for NMP recovery.

Parameter	Value	Source
Workers per shift	2	[71]
Energy consumption in kWh kg_{nmp}^{-1}	10.2	[87]
Invest in mio. $	15.0	[20]
Process rate in kg_{nmp} h^{-1}	1910	[71]
Ratio NMP:PVDF	19:1	[20]
Efficiency of recovery in %	99.5	[72]
Machine area in m^2	275	[71]

Table A.15
Parameterization of the PBCM for calendering.

Parameter	Value	Source
Workers per shift	0.5	[20]
Energy consumption in kWh	17	[20]
Invest in mio. $	5.35	[20]
Calender speed in m min^{-1}	68	[20,35,38,72,85]
Working width in mm	1000	Table A.13
Machine area in m^2	40	[20]

Table A.16
Parameterization of the PBCM for cutting.

Parameter	Value	Source
Workers per shift	0.5	[20]
Power consumption in kW	12	[20]
Invest in mio. $	1.55	[20]
Cutting speed in m min^{-1}	72	[20,35,84]
Working width in mm	1000	Table A.13
Machine area in m^2	27	[20]

Table A.17
Parameterization of the PBCM for vacuum drying.

Parameter	Value	Source
Workers per shift	4	[71]
Power consumption in kW	1296	[20]
Invest in mio. $	4.0	[71]
Dryers per machine	10	[71]
Process rate in m^2 h^{-1}	2500	[71]
Machine area in m^2	330	[71]

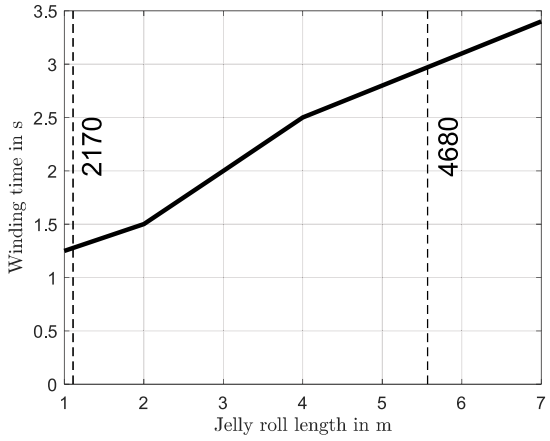

Fig. 9. Tabless winding time as a function of the jelly roll length. The values are based on the experience of Fraunhofer Institute for Manufacturing Engineering and Automaton IPA.

Calendering

Separate large calenders are used for anode and cathode to prevent cross contamination. Values for parameterization are taken from [20] based on a working width of 600 mm. In order to match the previous assumption for the working width of 1000 mm the values for the required plant area and the power consumption are scaled with a linear approach from 10 kW to 17 kW and from 24 m^2 to 40 m^2, respectively. For the calendering speed an average of 68 m min^{-1} is calculated based on a reported range between 30 m min^{-1} and 100 m min^{-1} in recent literature [20,35,38,72,85]. Due to the adapted working width and calendering speed to throughput increases from 18 m min^{-2} to 68 m min^{-2}. The invest is thus scaled with a linear approach to match the increased throughput from 1.42 mio $ to 5.35 mio $. Full parameterization is summarized in Table A.15.

Cutting

Cutting for anode and cathode is conducted via a roller scissor with ceramic knives. Parameterization is based on [20] and a working width of 600 mm. Due to a different assumption for the working width of 1000 mm the plant area and power consumption is scaled to match with the same linear approach as for the previous sections from 7 kW to 12 kW and from 16 m^2 to 27 m^2,respectively. Again for the cutting time an average of 72 m min^{-1} is calculated based on reported values of 50 m min^{-1} to 115 m min^{-1} in recent literature [20,35,84]. Due to the adapted working width and cutting speed the throughput increases from 30 m min^{-2} to 72 m min^{-2}. The invest is thus scaled with a linear approach to match the increased throughput from 0.65 mio. $ to 1.55 mio. $. Full parameterization is summarized in Table A.16.

Vacuum drying

For intensity drying a vacuum approach is assumed. This has the advantage that multiple electrode coils with multiple hundred meters of length may be dried simultaneously and low plant area requirements. Larger water diffusion coefficient is another advantage compared to drying under regular atmosphere [88]. Values for parameterization are taken from [20,71] as listed in Table A.17.

Tabless winding

The tabless winding time as a function of the jelly roll length is depicted in Fig. 9. The winding time includes the fixating of the electrode-separator stack at the beginning, the actual winding process and the ejection of the finished jelly roll. Marked is the jelly roll length of 1.11 m and 5.57 m for 2170 cells and 4680 cells with steel housing, respectively. This translates to winding times of 1.278 s and 2.971 s, respectively. The comparison of the correlating specific winding speed of 0.869 m s^{-1} (2170) and 1.875 m s^{-1} (4680) emphasizes the increased process rate for larger diameters.

Equipment for laser welding of collector plates

Characteristics of assumed continuous wave single-mode fiber laser:

- Laser source with high beam quality and good focus ability, possibility of pulse mode to ensure dynamic use response, long use stability, fiber diameter <= 50 μm

Table A.18
Parameterization of the PBCM for inserting the jelly roll into the can.

Parameter	Value	Source
Workers per shift	0.2	[20]
Power consumption in kW	5	[20]
Invest in mio. $	0.63	[22]
Process rate in pieces min^{-1}	35	[22]
Scrap loss in %	0.05	[20]
Machine area in m^2	5	[22]

Table A.19
Parameterization of the PBCM for electrolyte filling.

Parameter	Value	Source
Workers per shift	0.34	[20]
Power consumption in kW	20	[20]
Invest in mio. $	1.8	[22]
Filling speed in ml s^{-1}	0.5	[20]
Number of parallel filling channels	12	[20]
Machine area in m^2	6	[20]

- Exemplary manufacturers: IPG Laser GmbH & Co. KG (Burbach, Germany), TRUMPF Laser- und Systemtechnik GmbH (Ditzingen, Germany), Coherent, Inc. (Sante Clara, California)

Characteristics of assumed scanner optic:

- PFO with 2D positioning, high accuracy in positioning writing, F-Theta lense, optical interfaces to monitor process, spot diameter <= 70 µm
- Exemplary manufacturers: RAYLASE GmbH (Wessling, Germany), IPG Laser GmbH & Co. KG (Burbach, Germany), Precitec GmbH & Co. KG (Gaggenau, Germany), TRUMPF Laser- und Systemtechnik GmbH (Ditzingen, Germany), SCANLAB GmbH (Puchheim, Germany)

Characteristics of assumed clamping fixture:

- Clamping fixture: Positioning and clamping collector plates to jelly role, integrated into assembly line, high accuracy, uniform contact pressure

A.1.2. A2) Housing manufacturing

Complete parameterization in the main text.

A.1.3. B) Assembly

Insertion of jelly roll into can

After preparing the tabless jelly roll with joined connector and endcap, it is inserted into the can. Values for parameterization are based on [20,22] as listed in Table A.18

Electrolyte filling

For electrolyte filling a rotary table is assumed that can fill a number of cells at the same time. Different sources report different values for the invest cost for such types of machines [20,22]. Therefore, an average between the values is assumed. The filling speed is assumed as 0.5 ml s^{-1} independent of the dimensions. It is highly likely that this is a very rough estimation as we hypothesize the filling speed will be mainly a function of the cell height as the electrolyte has to travel a larger distance along the *z*-axis of the cell. Similar assumptions were formulated recently in other sources [79]. This is a possible source of error that has to be kept in mind when interpreting the results and an aspect that can be improved in future studies once this relationship is revealed in detail. Full parameterization is summarized in Table A.19.

Closing fill hole

The fill hole is closed by inserting and laser welding a small steel ball. Afterwards, the cell is sealed and protected against the atmosphere and subsequent steps can be performed outside of the dry room. Values for parameterization are taken from [20] while the process speed is again an average between [20,22] as listed in Table A.20.

Table A.20
Parameterization of the PBCM for closing of the fill hole.

Parameter	Value	Source
Workers per shift	0.2	[20]
Power consumption in kW	5	[20]
Invest in mio. $	0.53	[22]
Process rate in pieces min^{-1}	40	[20]
Scrap loss in %	0.05	[20]
Machine area in m^2	4	[20]

A.1.4. C) Finishing

Formation

Continuous parameterization of the formation step as a function of dimensions has not yet been reported in the literature to the best of our knowledge. A number of literature sources were used and combined with our own assumptions to establish reasonable parameterization.

For formation the cells are inserted into a cycler with an individual channel for each cell. The invest for the machine is primarily determined by the amount of channels required and the requirements of power consumption thereof. Larger cells require larger currents for a given C-rate which translates into higher power consumption per channel [20]. According to [89] the invest per channel can be linearly approximated with respect to the cell capacity. The invest for a formation machine with 140 cyclers and 1600 channels each amounts to 28 mio. $ [71]. This translates to 125 $ per channel for a cell with 67 Ah. For cells with more than 80 Ah the invest increases by 10% according to [71]. With the assumption of a linear relationship Eq. (31) is established to calculate the invest INV_{form} with C_{cell} as the cell capacity.

$$INV_{form} = 0.96 C_{cell} \frac{\$}{Ah} + 60.6\ \$ \tag{31}$$

The cell assumed in [71] is a pouch cell with 16.10 cm^2 area occupied in the cycler, for 1600 channels per cycler this equals an area of A_{cycler} = 2.576 m^2 which is provided for cells. Eq. (32) is assumed to calculate the number of tabless cylindrical cells $n_{cell,cycler}$ with the diameter d_{cell} that fit into this area while the cells are assumed to be arranged in a 90° angle. No dependence on the height is assumed. For operation of the cycler a control unit with a process rate of 50000 cells per day and an invest of 0.59 mio $ per control unit is used.

$$n_{cell,cycler} = \frac{A_{cycler}}{d_{cell}^2} \tag{32}$$

Energy consumption for the formation of one cell E_{form} as a function of the capacity is calculated according to Eq. (33) based on [90]. Here, $E_{chc,first}$ is the energy required for charging including the first cycle loss, E_{chc} is the energy required for regular charging and E_{dsc} is the energy released during discharging of the cell.

$$E_{form} = E_{chc,first} - E_{dsc} + E_{chc} - E_{dsc} + 0.5 E_{chc} \tag{33}$$

Eq. (33) assumes a formation protocol with two full charging and discharging cycles and a charge to 50% state of charge (SOC). The energy for a first cycle charge $E_{chc,first}$ and a regular cycle charge E_{chc} is calculated according to Eq. (34) and Eq. (35), respectively. The energy for a regular discharge E_{dsc} is calculated according to Eq. (36). Here, U_{nom} is the nominal voltage, $\eta_{CE,first}$ is the Coulomb efficiency of the first cycle and η_{cell} is the energy efficiency of the cell for the C-rate and environmental temperature assumed during formation. $\eta_{CE,first}$ is assumed as 87% and η_{cell} is assumed as 98%.

$$E_{chc,first} = \frac{C_{cell} U_{nom}}{\eta_{CE,first} \eta_{cell}} \tag{34}$$

Table A.21
Parameterization of the PBCM for formation.

Parameter	Value	Source
Workers per shift per cycler	0.036	[71]
Energy consumption in kWh cell^{-1}	1.1 $\frac{E_{form}}{J}$ (Eq. (33))	[90]
Invest in $ per channel	Eq. (31)	[71]
Invest control unit in $ cell^{-1}	11.8	[20]
Cells per cycler	Eq. (32)	[71]
Formation duration in h cell^{-1}	26	[20,35,91]
Scrap loss in %	0.5	[71]
Machine area in m^2 per cycler	1.375	[71]

Table A.22
Parameterization of the PBCM for aging and EOL check.

Parameter	Value	Source
Workers per shift per shelf	0.002	[71]
Power consumption in kW	50	[20]
Invest in $ per shelf	5555	[71]
Invest control unit in $ cell^{-1}	11.8	[20]
Cells per shelf	Eq. (32)	[71]
Aging duration in h cell^{-1}	336	[71]
Scrap loss in %	4.5	[71]
Machine area in m^2 per shelf	1.375	[71]

Table A.23
Parameterization of the PBCM for incoming.

Parameter	Value	Source
Workers per shift	5	[71]
Power consumption in kW	38.5	[20]
Invest in mio. $	8.0	[71]
Process rate in kg h^{-1}	7700	[71]
Machine area in m^2	880	[71]

Table A.24
Parameterization of the PBCM for shipping.

Parameter	Value	Source
Workers per shift	15	[71]
Power consumption in kW	41	[20]
Invest in mio. $	20.0	[71]
Process rate in kg h^{-1}	8200	[71]
Machine area in m^2	1375	[71]

Table A.25
Parameterization of the PBCM for the dry room.

Parameter	Value	Source
Workers per shift per m^{-2}	$\frac{1}{6100}$	[71]
Power consumption in kW day^{-1}m^{-2}	6.8	[20]
Invest in $ m^{-2}	1147	[71]

$$E_{chc} = \frac{C_{cell} U_{nom}}{\eta_{cell}} \tag{35}$$

$$E_{dsc} = C_{cell} U_{nom} \eta_{cell} \tag{36}$$

For the total energy consumption of the formation machine an additional 10% is assumed for the infrastructure in addition to the energy required for formation according to Eq. (33). Workers per shift are scaled linearly with the number of cyclers to 0.036. Formation duration is assumed to 26 h which is an average of values reported in the literature [20,35,91]. Full parameterization is summarized in as listed in Table A.21.

Aging and end of line check

Aging and end of line (EOL) check is done in a similar facility as formation but no current flow or supervision is necessary [71]. According to [71] a machine area of 990 m^2 or 1800 m^2 effective manufacturing area is required for this step. With the assumption of the same area of 2.576 m^2 as for the cyclers, this translates to 720 shelves. One aging machine with 720 shelves requires invest of 4.0 mio $ and 1.5 workers per shift [71]. Therefore, 5555 $ per shelf and 0.002 workers per shift per shelf are assumed. The number of cells per shelf is calculated identical to Eq. (32). Power consumption is mainly determined by the electronical aging management system. Therefore, the power consumption is scaled with the number of control units required and set to 50 kW.

In case a cell shows a strong aging behavior an internal short circuit is likely and those cells are scrapped. According to [71] a scrap loss of 5% for formation and aging combined is reasonable. As Table A.21 already assumes 0.5% scrap loss for formation another 4.5% is assumed for aging and EOL check according to Table A.22

A.1.5. Others

Incoming

Parameters for incoming are based on [71] with the assumption of two-shift operation and 5 workers per shift. No value for power consumption was given in [71], thus values from [20] are linearly scaled to match 7700 kg process rate from [71] as listed in Table A.23.

Shipping

Similar to incoming the parameters for shipping are based on [71] with the assumption of a power consumption of 10 kW per 2000 kg h^{-1} process rate from [20]. A process rate of 8200 kg h^{-1} from [71] thus yields a power consumption of 41 kW as listed in Table A.24.

Dry room

Winding, contacting of the collector plates and the whole cell assembly must be carried out in a dry room with humidity of less than 1%. The dry room generally is a large power consumer which is mainly determined by diffusion of steam through the walls, air intake through the air locks, the number of workers inside the room and the exchange of fresh air. Values for parameterization for a dry room with invest of 7 mio. $ and 6100 m^2 area are taken from [20,71] and scaled with the area as listed in Table A.25. The energy consumption is calculated based on the dry room area with 6.8 kWh day^{-1}m^{-2} [20].

A.2. Operations model

In this sections, the superscript ^{j} is added if the value refers to a specific manufacturing step j and the superscript ^{i} is added if the value refers to a specific material i. Values refer to annual values within a period of one year in which the annual output of E_{target}= 40 GWh is targeted.

A.2.1. Machinery, plant area, working hours and energy consumption

The required plant area, working hours and energy consumption are mainly determined by the total number of required machines to produce the annual output. The total number of machines $n^j_{mach,tot}$ required for manufacturing step j is calculated according to Eq. (37) with $n^j_{prod,tot}$ as the total annual required quantity of product in the respective measure and $n^j_{prod,machine}$ as the quantity of product a single machine can produce. As only an integer number of machines may be utilized the result is rounded up which means an underutilization of machines is considered in this study.

$$n^j_{mach,tot} = \lceil \frac{n^j_{prod,tot}}{n^j_{prod,machine}} \rceil \tag{37}$$

The total annual required quantity of product per manufacturing step j is calculated such that at the end of the manufacturing process the targeted annual output E_{target} is met. Due to inevitable scrap losses it might be necessary to produce a larger quantity of product for manufacturing step j than is eventually utilized in salable cells. First, the total required manufacturing volume of salable cells $n_{cell,salable,tot}$ at the end of the manufacturing process is calculated with Eq. (38). Here, E_{cell} is the energy content per cell calculated with the formulas from the geometrical model in Table 1. The manufacturing volume of salable cells is corrected by the scrap losses along the manufacturing process to calculate the actual total number of cells $n_{cell,manu,tot}$ the manufacturing must aim for according to Eq. (39). Here, S_p^k is the scrap loss for a specific manufacturing step k counted along all manufacturing steps, $k = 1...n_{steps}$. In general, $n_{cell,manu,tot}$ is always greater than $n_{cell,salable,tot}$.

$$n_{cell,salable,tot} = \frac{E_{target}}{E_{cell}} \tag{38}$$

$$n_{cell,manu,tot} = n_{cell,salable,tot} \frac{1}{\prod_{k=1}^{n_{steps}} (1 - S_p^k)} \tag{39}$$

The total required quantity of product $n^j_{prod,tot}$ for manufacturing step j is calculated according to Eq. (40) with $n_{cell,manu,tot}$ corrected by the scrap losses S_p^k occurring during all previous manufacturing steps, $k = 1...j-1$, meaning less relative quantity of product is required as the manufacturing progresses. In case the unit of measure for the output of a certain manufacturing step j is not a number of cells but a preliminary product, multiplication by the respective required quantity of preliminary product per cell M^j_{prelim} is necessary.

$$n^j_{prod,tot} = n_{cell,manu,tot} \prod_{k=1}^{j-1} (1 - S_p^k) M^j_{prelim} \tag{40}$$

The quantity of product $n^j_{prod,mach}$ a single machine can produce for manufacturing step j is calculated with Eq. (41) and the annual process rate PR^j. Here, n_{wdy} is the number of working days per year, n_{swd} is the number of shifts per working day, n_{whs} is the working hours per shift and MA^j is the percentage machine availability factor for the machines of manufacturing step j.

$$n^j_{prod,mach} = n_{wdy} n_{swd} n_{whs} PR^j \times MA^j \tag{41}$$

The total plant area $A^j_{mach,tot}$ for the required amount of machines to perform manufacturing step j is calculated with Eq. (42). Here, $n^j_{mach,tot}$ is the total number of machines according to Eq. (37) and A^j_{mach} is the required plant area for a single machine of manufacturing step j.

$$A^j_{mach,tot} = n^j_{mach,tot} A^j_{mach} \tag{42}$$

In some cases the last machine is not fully utilized for the given annual output which affects the power consumption and the working hours. Therefore, the overall percentage utilization of the last machine UT^j_{last} of manufacturing step j is calculated according to Eq. (43).

$$UT^j_{last} = \lceil \frac{n^j_{prod,tot}}{n^j_{prod,mach}} \rceil - \frac{n^j_{prod,tot}}{n^j_{prod,mach}} \tag{43}$$

The total amount of required working hours $n^j_{wh,tot}$ and energy E^j_{tot} of manufacturing step j can finally be calculated with Eq. (44) and Eq. (45), respectively. Here, n^j_{wm} is the required number of workers per machine and P^j_{mach} is the power consumption per machine.

$$n^j_{wh,tot} = (n^j_{mach,tot} - (1 - UT^j_{last})) n^j_{wm} n_{wdy} n_{swd} n_{whs} \tag{44}$$

$$E^j_{tot} = (n^j_{mach,tot} - (1 - UT^j_{last})) P^j_{mach} n_{wdy} n_{swd} n_{whs} \tag{45}$$

Table A.26
Scrap loss for different manufacturing steps. The values are identical with those reported in the respective tables for the individual manufacturing steps.

Manufacturing step j	Scrap loss in %	Type of scrap loss
Mixing	1	Anode material and cathode material
Winding	0.6	Tabless jelly rolls
Jelly roll insertion into can	0.05	Cell without electrolyte
Closing of fill hole	0.05	Finished cell
Formation	0.5	Finished cell
Aging and end of line check	4.5	Finished cell

A.2.2. Material

The required respective material masses for the targeted annual output are calculated with consideration of the required number of salable cells as well as scrap losses along the manufacturing process. First, the total material mass within the salable cells $m^i_{salable,tot}$ for each individual material i is calculated according to Eq. (46) with the number of salable cells from Eq. (38). Here, m^i_{cell} is the mass of material i per cell calculated with Eq. (23).

$$m^i_{salable,tot} = m^i_{cell} n_{cells,salable,tot} \tag{46}$$

The additional total scrap loss $m^i_{scrap,tot}$ for material i is calculated with Eq. (47). Here, $S_p^{i,k}$ is the percentage scrap loss for material i per manufacturing step k counted along all manufacturing steps, $k = 1...n_{steps}$, and $n_{cell,manu,tot}$ from Eq. (39). It is important to note that the actual type of scrap loss for each manufacturing step must be considered here. For instance, mixing has a percentage scrap loss of 1%, but this refers to pure raw anode material and cathode material. The closing of the fill hole produces only 0.05% scrap loss but this refers to complete cells that are wasted with all the material required up to this step. For easy overview Table A.26 summarizes the values of $S_p^{i,j}$. The values are identical with those already reported above for parameterization of each manufacturing step.

$$m^i_{scrap,tot} = n_{cell,manu,tot} (1 - \prod_{k=1}^{n_{steps}} (1 - S_p^{i,k})) m^i_{cell} \tag{47}$$

Finally, the total material mass m^i_{tot} for material i is the sum of the material masses present within the salable number of cells $m^i_{salable,tot}$ and the scrap losses $m^i_{scrap,tot}$ according to Eq. (48).

$$m^i_{tot} = m^i_{salable,tot} + m^i_{scrap,tot} \tag{48}$$

A.3. Financial model

A.3.1. Material

The total material cost $CO^i_{mat,tot}$ of material i along all manufacturing steps is calculated with Eq. (49). Here, m^i_{tot} is known from Eq. (48) and p^i is the respective material price for component i according to Table 11. Eq. (49) is formulated with the areas and volumes instead of the masses for the components which prices are given with respect to these values in Table 11. The total material cost $CO_{mat,tot}$ for all materials is calculated according to Eq. (50) as the sum of the material cost of all $n_{mat} = 18$ different materials present in the reference cell.

$$CO^i_{mat,tot} = m^i_{tot} p^i \tag{49}$$

$$CO_{mat,tot} = \sum_{i=1}^{n_{mat}} CO^i_{mat,tot} \tag{50}$$

A.3.2. Labor

The cost of labor is calculated based on the ERA EG 7 collective agreement for the metal and electrical industry in Baden-Württemberg, Germany [92] in 2021. The values reported in ERA EG 7 represent the gross wage for workers. Additional cost for the employer arises for example from social security payments. It is assumed the true cost for

Table A.27
Labor cost for parameterization of the financial model for the year 2021.

ERA paygroup	ERA gross wage in \$ year^{-1}	Total cost for employer in \$ year^{-1}	Labor cost in \$ h^{-1}
EG 7	45 885.48	78 005.3	53.06

the employer is 1.7 times larger than the value stated in ERA EG 7 [20]. Table A.27 summarizes the assumptions that lead to a specific cost of labor $CO_{lab,spc}$ = 53.06 \$ h^{-1} based on a 7 working hour shift, 210 working days per year and worker and thus 1470 working hours per year per worker. The original source reports wages in EUR [92] which are converted to \$ with the average exchange rate of 2021. The total cost of labor $CO^{j}_{lab,tot}$ per manufacturing step j is calculated according to Eq. (51) with the total required working hours n^{j}_{wh} known from Eq. (44).

$$CO^{j}_{lab,tot} = n^{j}_{wh,tot} CO_{lab,spc} \tag{51}$$

A.3.3. Capital

The cost of capital refers to the cost that arises with providing the capital for use within a business. As the required capital could be invested into the capital market with a given interest rate, the cost of capital considers the opportunity cost of the capital invested into the business.

The cost of capital CO_{cap} is calculated with the average bound capital within the business BC calculated with the assumption of linear reduction of the difference between the initial invest INV and the residual worth RW at the end of the service life according to Eq. (52). The average bound capital is then multiplied with an interest rate IR according to Eq. (53).

$$BC = \frac{INV + RW}{2} \tag{52}$$

$$CO_{cap} = BC \times IR \tag{53}$$

As interest rate the Weighted Average Cost of Capital (WACC) is assumed which represents the average cost of equity capital and borrowed capital for a business [93]. The WACC is assumed as 7.6% which represents an average value within the automotive industry in 2021 [94]. The residual worth of the machines is assumed as 10% of the invest [20]. The total cost of capital $CO^{j}_{cap,tot}$ for manufacturing step j is then calculated according to Eq. (54) with the invest per machine INV^{j}_{mach} and the number of machines $n^{j}_{mach,tot}$ known from Eq. (37).

$$CO^{j}_{cap,tot} = \frac{(1.0 + 0.1) INV^{j}_{mach}}{2} n^{j}_{mach,tot} WACC \tag{54}$$

A.3.4. Depreciation

Depreciation refers to the continuous value reduction of the fixed assets and represents the yearly reserves required to be able to reinvest into a new machine at the end of the service life. There are different methods to calculate the depreciation while the linear method is most commonly used.

The calculation should be based on the expected cost of reinvest $RINV$ into the machines [20]. The cost of depreciation CO_{depr} per machine is thus calculated with Eq. (55) with the linear method. Here, n_{depr} is the number of periods assumed for the depreciation.

$$CO_{depr} = \frac{RINV - RW}{n_{depr}} \tag{55}$$

For parameterization of Eq. (55) it is assumed the reinvest for the machines is 110% of the initial invest due to inflation [20] while the residual worth in 10% of the invest. Service life SL of the machines is assumed to be eight years [20]. The total cost of depreciation $CO^{j}_{depr,tot}$ for manufacturing step j is then calculated with Eq. (56) by multiplying with the number of machines $n^{j}_{mach,tot}$ known from Eq. (37).

$$CO^{j}_{depr,tot} = \frac{(1.1 - 0.1) INV^{j}_{mach}}{SL} n^{j}_{mach,tot} \tag{56}$$

A.3.5. Energy

Cost of energy is calculated based on an average specific price for electrical energy including taxes for the German industry of p_{energy} =0.2523 \$ kWh^{-1} (0.2138 EUR kWh^{-1}) according to the 'Bundesverband der Energie- und Wasserwirtschaft e.V. (BDEW)' [95]. For each manufacturing step j the total cost of energy $CO^{j}_{enery,tot}$ is then calculated with Eq. (57) and the total amount of energy required E^{j}_{tot} known from Eq. (45).

$$CO^{j}_{energy,tot} = E^{j}_{tot} p_{energy} \tag{57}$$

A.3.6. Area

According to the German ministry of statistics construction prices for factories averaged at 1450.22 \$ m^{-2} (1229 EUR m^{-2}) in 2021 [96]. Land for commercial use could be purchased for 110.75 \$ m^{-2}(93.86 EUR m^{-2}) [97]. For buildings a depreciation period of 50 years is assumed [20]. Considering a WACC of 7.6% the capital cost calculates to 59.32 \$ m^{-2} according to Eq. (54) and the depreciation calculates to 31.22 \$ m^{-2} according to Eq. (56). For yearly maintenance 1% of the construction and land cost is assumed [20] which calculates to 15.61 \$ m^{-2}. Baseline energy consumption for electricity, heat and lighting is assumed as 5 W m^{-2}. Based on 300 working days per year and the assumed specific cost of energy of p_{energy} = 0.2523 \$ kWh^{-1} this equals 9.09 \$ m^{-2}. The total cost of area calculates to 115.23 \$ m^{-2} with respect to the plant area. The total required plant area is assumed as 440% of the manufacturing area [20] which translates to specific cost per manufacturing area of $CO_{area,spc}$ = 507 \$ m$^{-2}_{manu}$. The total cost of area $CO^{j}_{area,tot}$ for manufacturing step j is finally calculated according to Eq. (58) with the required manufacturing area for machines $A^{j}_{mach,tot}$ from Eq. (42).

$$CO^{j}_{area,tot} = A^{j}_{mach,tot} CO_{area,spc} \tag{58}$$

A.3.7. Maintenance and overhead

According to [22] for manufacturing of cylindrical cells an additional 10% can be assumed for total cost of maintenance $CO^{j}_{maint,tot}$ with respect to the total cost of depreciation according to Eq. (59) with $CO^{j}_{depr,tot}$ known from Eq. (56). For total overhead cost $CO^{j}_{overh,tot}$ 33% can be assumed with respect to the total cost of maintenance, cost of depreciation and cost of area [17] according to Eq. (60) with $CO^{j}_{area,tot}$ known from Eq. (58).

$$CO^{j}_{maint,tot} = 0.1 CO^{j}_{depr,tot} \tag{59}$$

$$CO^{j}_{overh,tot} = 0.33 (CO^{j}_{maint,tot} + CO^{j}_{depr,tot} + CO^{j}_{area,tot}) \tag{60}$$

References

[1] Tesla, Tesla battery day presentation deck, 2020, URL: https://tesla-share.thron.com/content/?id=96ea71cf-8fda-4648-a62c-753af436c3b6&pkey=S1dbei4.

[2] K. Tsuruta, M.E. Dermer, R. Dhiman, A Cell with A Tabless Electrode, (EP3878029 (A1)) Tesla Inc, 2021.

[3] T.G. Tranter, R. Timms, P.R. Shearing, D.J.L. Brett, Communication—Prediction of thermal issues for larger format 4680 cylindrical cells and their mitigation with enhanced current collection, J. Electrochem. Soc. 167 (16) (2020) 160544, http://dx.doi.org/10.1149/1945-7111/abd44f.

[4] J. Sturm, A. Frank, A. Rheinfeld, S.V. Erhard, A. Jossen, Impact of electrode and cell design on fast charging capabilities of cylindrical lithium-ion batteries, J. Electrochem. Soc. 167 (13) (2020) 130505, http://dx.doi.org/10.1149/1945-7111/abb40c.

[5] K.-J. Lee, K. Smith, A. Pesaran, G.-H. Kim, Three dimensional thermal-, electrical-, and electrochemical-coupled model for cylindrical wound large format lithium-ion batteries, J. Power Sources 241 (2013) 20–32, http://dx.doi.org/10.1016/j.jpowsour.2013.03.007.

[6] S. Li, N. Kirkaldy, C. Zhang, K. Gopalakrishnan, T. Amietszajew, L.B. Diaz, J.V. Barreras, M. Shams, X. Hua, Y. Patel, G.J. Offer, M. Marinescu, Optimal cell tab design and cooling strategy for cylindrical lithium-ion batteries, J. Power Sources 492 (2021) 229594, http://dx.doi.org/10.1016/j.jpowsour.2021.229594.

[7] H. Pegel, D. Wycisk, A. Scheible, L. Tendera, A. Latz, D.U. Sauer, Fast-charging performance and optimal thermal management of large-format full-tab cylindrical lithium-ion cells under varying environmental conditions, J. Power Sources 556 (2023) 232408, http://dx.doi.org/10.1016/j.jpowsour.2022.232408.

[8] L. Tendera, H. Pegel, C. Gonzalez, D. Wycisk, A. Fill, K.P. Birke, Influence of temperature, state of charge and state of health on the thermal parameters of lithium-ion cells: Exploring thermal behavior and enabling fast-charging, Future Batter. 1 (2024) 100001, http://dx.doi.org/10.1016/j.fub.2024.100001.

[9] H. Pegel, D. Wycisk, D.U. Sauer, Influence of cell dimensions and housing material on the energy density and fast-charging performance of tabless cylindrical lithium-ion cells, Energy Storage Mater. 60 (2023) 102796, http://dx.doi.org/10.1016/j.ensm.2023.102796.

[10] Reuters, Board member says BMW to cut production cost per vehicle by 25%, 2021, URL: https://www.reuters.com/business/autos-transportation/board-member-says-bmw-cut-production-cost-per-vehicle-by-25-2021-06-21/.

[11] BMW Group AG, More performance, CO2-reduced production, significantly lower costs: BMW group to use innovative round BMW battery cells in NEUE KLASSE from 2025, 2022, URL: https://www.press.bmwgroup.com/global/article/detail/T0403470EN/more-performance-co2-reduced-production-significantly-lower-costs:-bmw-group-to-use-innovative-round-bmw-battery-cells-in-neue-klasse-from-2025?language=en.

[12] BMW Group AG, Round battery cells for the Neue Klasse, 2022, URL: https://www.bmwgroup.com/en/news/general/2022/gen6.html.

[13] M. Kane, Rumor: Samsung SDI developing various 4680 cylindrical batteries, 2022, URL: https://insideevs.com/news/589164/samsung-sdi-develops-4680-batteries/.

[14] M. Kane, BAK battery unveils first Chinese 4680 battery cells, 2021, URL: https://insideevs.com/news/497176/bak-battery-unveils-first-4680-cells-china/.

[15] C. Randall, Rimac announces more energy-dense battery development, 2022, URL: https://www.electrive.com/2022/07/29/rimac-announces-more-energy-dense-battery-development/.

[16] S. Doll, Rimac follows Tesla in developing 46mm battery cells, but at 'varied heights' beyond 80mm, 2022, URL: https://electrek.co/2022/07/18/rimac-tesla-46mm-battery-cells/.

[17] F. Duffner, L. Mauler, M. Wentker, J. Leker, M. Winter, Large-scale automotive battery cell manufacturing: Analyzing strategic and operational effects on manufacturing costs, Int. J. Prod. Econ. 232 (2021) 107982, http://dx.doi.org/10.1016/j.ijpe.2020.107982.

[18] M. Wentker, M. Greenwood, J. Leker, A bottom-up approach to lithium-ion battery cost modeling with a focus on cathode active materials, Energies 12 (3) (2019) 504, http://dx.doi.org/10.3390/en12030504.

[19] M. Greenwood, M. Wentker, J. Leker, A bottom-up performance and cost assessment of lithium-ion battery pouch cells utilizing nickel-rich cathode active materials and silicon-graphite composite anodes, J. Power Sources Adv. 9 (2021) 100055, http://dx.doi.org/10.1016/j.powera.2021.100055.

[20] J.-H. Schünemann, Modell zur Bewertung der Herstellkosten von Lithiumionenbatteriezellen, in: IPAT-Schriftenreihe, Bd. 16, Sierke, Göttingen, 2015, 1. Aufl..

[21] A. Sakti, J.J. Michalek, E.R. Fuchs, J.F. Whitacre, A techno-economic analysis and optimization of Li-ion batteries for light-duty passenger vehicle electrification, J. Power Sources 273 (2015) 966–980, http://dx.doi.org/10.1016/j.jpowsour.2014.09.078.

[22] R.E. Ciez, J.F. Whitacre, Comparison between cylindrical and prismatic lithium-ion cell costs using a process based cost model, J. Power Sources 340 (2017) 273–281, http://dx.doi.org/10.1016/j.jpowsour.2016.11.054.

[23] R.J. Brodd, C. Helou, Cost comparison of producing high-performance Li-ion batteries in the U.S. and in China, J. Power Sources 231 (2013) 293–300, http://dx.doi.org/10.1016/j.jpowsour.2012.12.048.

[24] J.B. Quinn, T. Waldmann, K. Richter, M. Kasper, M. Wohlfahrt-Mehrens, Energy density of cylindrical li-ion cells: A comparison of commercial 18650 to the 21700 cells, J. Electrochem. Soc. 165 (14) (2018) A3284–A3291, http://dx.doi.org/10.1149/2.0281814jes.

[25] T. Waldmann, R.-G. Scurtu, D. Brändle, M. Wohlfahrt-Mehrens, Effects of tab design in 21700 Li–Ion cells: Improvements of cell impedance, rate capability, and cycling aging, Energy Technol. 11 (5) (2023) http://dx.doi.org/10.1002/ente.202200583.

[26] M.F. Börner, A.M. Mohsseni, N. De, M. Faber, F. Krause, W. Li, S. Bihn, F. Ringbeck, D.U. Sauer, Manufacturing cost comparison of tabless vs. standard electrodes for cylindrical lithium-ion batteries, J. Energy Storage 77 (2024) 109941, http://dx.doi.org/10.1016/j.est.2023.109941.

[27] H. Pegel, M. Autenrieth, S. Schaeffler, A. Jossen, D.U. Sauer, Design guidelines to prevent thermal propagation and maximize packing density within battery systems with tabless cylindrical lithium-ion cells, J. Energy Storage 86 (2024) 111275, http://dx.doi.org/10.1016/j.est.2024.111275.

[28] W. Li, K.R. Crompton, C. Hacker, J.K. Ostanek, Comparison of current interrupt device and vent design for 18650 format lithium-ion battery caps, J. Energy Storage 32 (2020) 101890, http://dx.doi.org/10.1016/j.est.2020.101890.

[29] H. Pegel, S. Schaeffler, A. Jossen, D.U. Sauer, Extensive experimental thermal runaway and thermal propagation characterization of large-format tabless cylindrical lithium-ion cells with aluminum housing and laser welded endcaps, J. Electrochem. Soc. 170 (12) (2023) 120512, http://dx.doi.org/10.1149/1945-7111/ad0cd3.

[30] M. Ank, A. Sommer, K. Abo Gamra, J. Schöberl, M. Leeb, J. Schachtl, N. Streidel, S. Stock, M. Schreiber, P. Bilfinger, C. Allgäuer, P. Rosner, J. Hagemeister, M. Rößle, R. Daub, M. Lienkamp, Lithium-ion cells in automotive applications: Tesla 4680 cylindrical cell teardown and characterization, J. Electrochem. Soc. 170 (12) (2023) 120536, http://dx.doi.org/10.1149/1945-7111/ad14d0.

[31] S. Baazouzi, N. Feistel, J. Wanner, I. Landwehr, A. Fill, K.P. Birke, Design, properties, and manufacturing of cylindrical li-ion battery cells—A generic overview, Batteries 9 (6) (2023) 309, http://dx.doi.org/10.3390/batteries9060309.

[32] S. Li, M.W. Marzook, C. Zhang, G.J. Offer, M. Marinescu, How to enable large format 4680 cylindrical lithium-ion batteries, Appl. Energy 349 (2023) 121548, http://dx.doi.org/10.1016/j.apenergy.2023.121548.

[33] J. Sturm, A. Frank, A. Rheinfeld, S.V. Erhard, A. Jossen, Impact of electrode and cell design on fast charging capabilities of cylindrical lithium-ion batteries, J. Electrochem. Soc. 167 (13) (2020) 130505, http://dx.doi.org/10.1149/1945-7111/abb40c.

[34] C.-H. Chen, F. Brosa Planella, K. O'Regan, D. Gastol, W.D. Widanage, E. Kendrick, Development of experimental techniques for parameterization of multi-scale lithium-ion battery models, J. Electrochem. Soc. 167 (8) (2020) 080534, http://dx.doi.org/10.1149/1945-7111/ab9050.

[35] H.H. Heimes, A. Kampker, C. Lienemann, M. Locke, C. Offermanns, S. Michaelis, E. Rahimzei, Lithium-Ion Battery Cell Production Process, PEM der RWTH Aachen University and DVMA, Aachen and Frankfurt am Main, 2018, URL: http://www.pem.rwth-aachen.de/global/show_document.asp?id=aaaaaaaaabdqbtk.

[36] Tesla, Inc, Tesla 4680 cell manufacturing line, 2022, URL: https://www.youtube.com/watch?v=ZLzjkWxqmmg.

[37] X. Zhang, T. Wierzbicki, Characterization of plasticity and fracture of shell casing of lithium-ion cylindrical battery, J. Power Sources 280 (2015) 47–56, http://dx.doi.org/10.1016/j.jpowsour.2015.01.077.

[38] A. Kwade, J. Diekmann, Recycling of Lithium-Ion Batteries, Springer International Publishing, Cham, 2018, http://dx.doi.org/10.1007/978-3-319-70572-9.

[39] K. Natori, H. Utsunomiya, T. Tanaka, Forming of thin-walled cylindrical cup by impact backward extrusion of Al-Si alloys processed by semi-solid cast and ECAP, J. Mater. Process. Technol. 297 (2021) 117277, http://dx.doi.org/10.1016/j.jmatprotec.2021.117277.

[40] R.E. Kirchain, Cost modeling of materials and manufacturing processes, in: Encyclopedia of Materials: Science and Technology, Elsevier, 2001, pp. 1718–1727, http://dx.doi.org/10.1016/B0-08-043152-6/00310-7.

[41] F. Field, R. Kirchain, R. Roth, Process cost modeling: Strategic engineering and economic evaluation of materials technologies, JOM 59 (10) (2007) 21–32, http://dx.doi.org/10.1007/s11837-007-0126-0.

[42] M. Kane, Panasonic announces 4680 battery cell production in Japan, 2022, URL: https://insideevs.com/news/570361/panasonic-annocuned-4680battery-production-japan/.

[43] C. Randall, LG to supply 4680 battery cells for Tesla, 2021, URL: https://www.electrive.com/2021/03/10/lg-to-supply-4680-battery-cells-for-tesla/.

[44] Kloeckner & Co Deutschland GmbH, EN AW-3003, 2022, URL: https://facts.kloeckner.de/werkstoffe/aluminium/en-aw-3003/.

[45] A. Das, R. Beaumont, I. Masters, P. Haney, Macro-modelling of laser micro-joints for understanding joint strength in electric vehicle battery interconnects, Materials (Basel, Switzerland) 14 (13) (2021) http://dx.doi.org/10.3390/ma14133552.

[46] N.N. Greenwood, A. Earnshaw, Chemie der Elemente, VCH, Weinheim, 1990, 1. Aufl., 1. korrigierter Nachdr. 1990 der 1. Aufl. 1988.

[47] Carl Roth GmbH + Co KG, Sicherheitsdatenblatt - Carboxymethylcellulose Natriumsalz ≥98 %, granuliert, 2021, URL: https://www.carlroth.com/de/de/von-a-bis-z/carboxymethylcellulose-natriumsalz/p/6190.1.

[48] M.H. Harandi, F. Alimoradi, G. Rowshan, M. Faghihi, M. Keivani, M. Abadyan, Morphological and mechanical properties of styrene butadiene rubber/nano copper nanocomposites, Results Phys. 7 (2017) 338–344, http://dx.doi.org/10.1016/j.rinp.2016.11.022.

[49] G.A. Joyce, W.M. Henry, A.W. Thornton, J.C. Hodgin, Carbon Black Intra-Aggregate Void Volume from Dynamic Compression Measurements, 244 ed., 2011, URL: https://www.micromeritics.com/Repository/Files/Ruber_World_Article_-_Carbon_Black_-_DVVA.pdf,

[50] S.H. Kim, G.W. Mulholland, M.R. Zachariah, Density measurement of size selected multiwalled carbon nanotubes by mobility-mass characterization, Carbon 47 (5) (2009) 1297–1302, http://dx.doi.org/10.1016/j.carbon.2009.01.011.

[51] G. Drossel, S. Friedrich, W. Huppatz, C. Kammer, W. Lehnert, O. Liesenberg, W. Mader, M. Paul, A. Rudolf, W. Thate, M. Ullmann, H.-W. Wenglorz, S. Zeltner, Aluminium-Taschenbuch, in: Praxis, Beuth Verlag GmbH, Deutsches Institut für Normung, Berlin, Wien, Zürich, 2018, 17. Auflage. URL: http://www.beuth.de/de/publikation/aluminium-taschenbuch-band-2/245248960.

[52] S. Ebnesajjad, Fluoropolymer Applications in Chemical Processing Industries: the Definitive User's Guide and Databook, second ed., in: Plastics Design Library, William Andrew Publishing, 2017, URL: http://www.sciencedirect.com/science/book/9780323447164.

[53] D.A. Blackadder, P.A. Lewell, The density of polyethylene single crystals, Polymer 9 (1968) 249–263, http://dx.doi.org/10.1016/0032-3861(68)90036-0.

[54] Y. Wang, Q. Wang, Y. Lan, Z. Song, J. Luo, X. Wei, F. Sun, Z. Yue, C. Yin, L. Zhou, X. Li, Aqueous aluminide ceramic coating polyethylene separators for lithium-ion batteries, Solid State Ion. 345 (2020) 115188, http://dx.doi.org/10.1016/j.ssi.2019.115188.

[55] Sigma-Aldrich Chemie GmbH, Safety Data Sheet - Dimethyl carbonat, 2022, URL: https://www.sigmaaldrich.com/DE/de/product/sial/517127.

[56] Sigma-Aldrich Chemie GmbH, Safety Data Sheet - Ethylencarbonat, 2022, URL: https://www.sigmaaldrich.com/DE/de/product/sial/676802.

[57] Sigma-Aldrich Chemie GmbH, Safety Data Sheet - Ethyl methyl carbonate, 2022, URL: https://www.sigmaaldrich.com/DE/de/product/aldrich/754935.

[58] Sigma-Aldrich Chemie GmbH, Safety data sheet - fluoroethylene carbonate, 2022, URL: https://www.sigmaaldrich.com/DE/de/product/aldrich/757349.

[59] Sigma-Aldrich Chemie GmbH, Safety data sheet - vinylene carbonate, 2022, URL: https://www.sigmaaldrich.com/DE/de/product/aldrich/809977.

[60] L. Mayr, L. Tomcic, M.K. Kick, C. Wunderling, M.F. Zaeh, Contacting of cylindrical lithium-ion batteries using short pulse laser beam welding, in: Lasers in Manufacturing Conference, 2021, URL: https://wlt.de/sites/default/files/2021-10/joining_welding_brazing/Contribution_292_final.pdf.

[61] H. Mohseni, M. Schmoeller, M.F. Zaeh, A novel approach for welding metallic foils using pulsed laser radiation in the field of battery production, in: Lasers in Manufacturing Conference, 2019, URL: https://api.semanticscholar.org/CorpusID:213068127.

[62] E. Kaiser, S. Pricking, C. Stolzenburg, A. Killi, Sputter-free and reproducible laser welding of electric or electronic copper contacts with a green laser, in: Lasers in Manufacturing Conference, 2015, URL: https://www.wlt.de/lim/Proceedings2015/Stick/PDF/Contribution123_final.pdf.

[63] A. Ascari, E.P. Zapico, V. Dimatteo, A. Fortunato, Dissimilar laser welding of copper and stainless-steel thin sheets for e-mobility applications, Procedia CIRP 111 (2022) 770–773, http://dx.doi.org/10.1016/j.procir.2022.08.125.

[64] E. Haddad, J. Helm, A. Olowinsky, A. Gillner, Nanosecond pulsed fiber laser as a tool for laser micro welding, Procedia CIRP 94 (2020) 571–576, http://dx.doi.org/10.1016/j.procir.2020.09.077.

[65] F. Kaufmann, J. Ermer, A. Maier, S. Roth, M. Schmidt, Influence of plume attenuation under high power laser welding of copper using visible wavelengths, J. Laser Appl. 33 (4) (2021) 1–9, http://dx.doi.org/10.2351/7.0000505.

[66] F.W. Müller, A. Schiebahn, U. Reisgen, Quality prediction of disturbed ultrasonic metal welds, J. Adv. Join. Processes 5 (2022) 100086, http://dx.doi.org/10.1016/j.jajp.2021.100086.

[67] C. Prieto, E. Vaamonde, D. Diego-Vallejo, J. Jimenez, B. Urbach, Y. Vidne, E. Shekel, Dynamic laser beam shaping for laser aluminium welding in e-mobility applications, Procedia CIRP 94 (2020) 596–600, http://dx.doi.org/10.1016/j.procir.2020.09.084.

[68] M. Möller, S. Vogt, Novel multi focus optic approach for gas-tight welding of aluminum alloys in e-mobility, Procedia CIRP 111 (2022) 774–777, http://dx.doi.org/10.1016/j.procir.2022.08.126.

[69] T. Sun, P. Franciosa, M. Sokolov, D. Ceglarek, Challenges and opportunities in laser welding of 6xxx high strength aluminium extrusions in automotive battery tray construction, Procedia CIRP 94 (2020) 565–570, http://dx.doi.org/10.1016/j.procir.2020.09.076.

[70] M.C. Asaba, F. Duffner, F. Frieden, J. Leker, S. von Delft, Location choice for large–scale battery manufacturing plants: Exploring the role of clean energy, costs, and knowledge on location decisions in Europe, J. Ind. Ecol. 26 (4) (2022) 1514–1527, http://dx.doi.org/10.1111/jiec.13292.

[71] P.A. Nelson, S. Ahmed, K.G. Gallagher, D.W. Dees, Modeling the Performance and Cost of Lithium-Ion Batteries for Electric-Drive Vehicles, third ed., 2019, http://dx.doi.org/10.2172/1503280.

[72] K. Knehr, J. Kubal, P. Nelson, S. Ahmed, Battery performance and cost modeling for electric-drive vehicles (A manual for BatPaC v5.0), 2022, http://dx.doi.org/10.2172/1877590.

[73] DEKRA, Preismonitor januar 2022, 2022, URL: https://www.bgr.bund.de/DERA/DE/Aktuelles/Monitore/2022/01-22/2022-01-preismonitor.pdf?_blob=publicationFile&v=3.

[74] R. Schmuch, R. Wagner, G. Hörpel, T. Placke, M. Winter, Performance and cost of materials for lithium-based rechargeable automotive batteries, Nat. Energy 3 (4) (2018) 267–278, http://dx.doi.org/10.1038/s41560-018-0107-2.

[75] Z. Du, J. Li, M. Wood, C. Mao, C. Daniel, D.L. Wood, Three-dimensional conductive network formed by carbon nanotubes in aqueous processed NMC electrode, Electrochim. Acta 270 (2018) 54–61, http://dx.doi.org/10.1016/j.electacta.2018.03.063.

[76] Deutsche Bundesbank, Exchange rate statistics, 2024, URL: https://www.bundesbank.de/resource/blob/810486/a6f85aac3ac47b07ea32eae66e4bfa82/mL/ii-euro-referenzkurse-der-ezb-data.pdf.

[77] C. Neef, Development perspectives for lithium-ion battery cell formats, 2022, URL: https://www.isi.fraunhofer.de/content/dam/isi/dokumente/cct/2022/Development_perspectives_for_lithium-ion_battery_cell_formats_Fraunhofer_2022.pdf.

[78] V. Henze, Battery pack prices fall to an average of $132/kWh, but rising commodity prices start to bite, 2021, URL: https://about.bnef.com/blog/battery-pack-prices-fall-to-an-average-of-132-kwh-but-rising-commodity-prices-start-to-bite/.

[79] C. Neef, Potenziale von 46-mm-Rundzellen, 2023, URL: https://www.isi.fraunhofer.de/de/blog/themen/batterie-update/46-mm-rundzellen-potenziale-standardformat-batteriezellen.html.

[80] AutoTech News, Nio unveils ET9 to take on Mercedes Maybach, deliveries to begin in Q1 2025, 2024, URL: https://autotech.news/nio-unveils-et9-to-take-on-mercedes-maybach/.

[81] Nio Inc., NIO day 2023 held in Xi'an, smart electric executive flagship ET9 unveiled, 2023, URL: https://www.nio.com/news/nio-day-2023?&noredirect=.

[82] C. Westerheide, Samsung SDI will supply cylindrical battery cells to GM, 2023, URL: https://www.electrive.com/2023/03/08/samsung-sdi-will-supply-cylindrical-battery-cells-to-gm/.

[83] Y. Bi, Q. Li, R. Yi, J. Xiao, To pave the way for large-scale electrode processing of moisture-sensitive Ni-rich cathodes, J. Electrochem. Soc. 169 (2) (2022) 020521, http://dx.doi.org/10.1149/1945-7111/ac4e5d.

[84] Duerr AG, Advanced battery electrode development and manufacturing, 2019, URL: https://www.durr.com/fileadmin/durr.com/04_Company/01_Events/2019/duerr-advanced-battery-brochure.pdf.

[85] C.A. Heck, M.-W. von Horstig, F. Huttner, J.K. Mayer, W. Haselrieder, A. Kwade, Review—Knowledge-based process design for high quality production of NCM811 cathodes, J. Electrochem. Soc. 167 (16) (2020) 160521, http://dx.doi.org/10.1149/1945-7111/abcd11.

[86] D.L. Wood, J.D. Quass, J. Li, S. Ahmed, D. Ventola, C. Daniel, Technical and economic analysis of solvent-based lithium-ion electrode drying with water and NMP, Drying Technol. 36 (2) (2018) 234–244, http://dx.doi.org/10.1080/07373937.2017.1319855.

[87] S. Ahmed, P.A. Nelson, D.W. Dees, Study of a dry room in a battery manufacturing plant using a process model, J. Power Sources 326 (2016) 490–497, http://dx.doi.org/10.1016/j.jpowsour.2016.06.107.

[88] F. Huttner, A. Marth, J.C. Eser, T. Heckmann, J. Mohacsi, J.K. Mayer, P. Scharfer, W. Schabel, A. Kwade, Design of vacuum post–drying procedures for electrodes of lithium–Ion batteries, Batter. Supercaps 4 (9) (2021) 1499–1515, http://dx.doi.org/10.1002/batt.202100088.

[89] J. Schnell, H. Knörzer, A.J. Imbsweiler, G. Reinhart, Solid versus liquid—A bottom–up calculation model to analyze the manufacturing cost of future high–energy batteries, Energy Technol. 8 (3) (2020) http://dx.doi.org/10.1002/ente.201901237.

[90] J.B. Dunn, L. Gaines, M. Barnes, M. Wang, J. Sullivan, Material and energy flows in the materials production, assembly, and end-of-life stages of the automotive lithium-ion battery life cycle, 2012, http://dx.doi.org/10.2172/1044525.

[91] C. Mao, S.J. An, H.M. Meyer, J. Li, M. Wood, R.E. Ruther, D.L. Wood, Balancing formation time and electrochemical performance of high energy lithium-ion batteries, J. Power Sources 402 (2018) 107–115, http://dx.doi.org/10.1016/j.jpowsour.2018.09.019.

[92] IG Metall, Tariftabellen Metall- und Elektroindustrie, 2022, URL: https://www.igmetall.de/tarif/tariftabellen/metall-und-elektroindustrie.

[93] M.Z. Frank, T. Shen, Investment and the weighted average cost of capital, J. Financ. Econ. 119 (2) (2016) 300–315, http://dx.doi.org/10.1016/j.jfineco.2015.09.001.

[94] S. Schoeniger, A. Tschoepel, Cost of capital study 2022, 2022, URL: https://kpmg.com/de/en/home/insights/2021/10/cost-of-capital-study-2021.html.

[95] Bundesverband der Energie- und Wasserwirtschaft, BDEW-Strompreisanalyse Dezember 2023, 2023, URL: https://www.bdew.de/service/daten-und-grafiken/bdew-strompreisanalyse/.

[96] Statistisches Bundesamt Destatis, Bauen und Wohnen: Baugenehmigungen Baukosten, 2022, URL: https://www.destatis.de/DE/Themen/Branchen-Unternehmen/Bauen/Publikationen/Downloads-Bautaetigkeit/baugenehmigungen-baukosten-pdf-5311103.pdf?_blob=publicationFile.

[97] Statistisches Bundesamt Destatis, Statistik der Kaufwerte für Bauland, 2023, URL: https://www-genesis.destatis.de/genesis/online?operation=statistic&levelindex=0&levelid=1705919873073&code=61511#abreadcrumb.